

# Accurately model the Kuramoto–Sivashinsky dynamics with holistic discretisation

T. MacKenzie\*      A. J. Roberts†

March 23, 2005 — without figures.

See

<http://www.sci.usq.edu.au/staff/aroberts/ksdoc.pdf> to  
download a version with the figures

## Abstract

We analyse the nonlinear Kuramoto–Sivashinsky equation to develop accurate discretisations modeling its dynamics on coarse grids. The analysis is based upon centre manifold theory so we are assured that the discretisation accurately models the dynamics and may be constructed systematically. The theory is applied after dividing the physical domain into small elements by introducing isolating internal boundaries which are later removed. Comprehensive numerical solutions and simulations show that the holistic discretisations excellently reproduce the steady states and the dynamics of the Kuramoto–Sivashinsky equation. The Kuramoto–Sivashinsky equation is used as an example to show how holistic discretisation may be successfully applied to fourth order, nonlinear, spatio-temporal dynamical systems. This novel centre manifold approach is holistic in the sense that it treats the dynamical equations as a whole, not just as the sum of separate terms.

**Keywords:** Kuramoto–Sivashinsky equation, low-dimensional modelling, computational discretisations

---

\*Department of Mathematics and Computing, University of Southern Queensland, Toowoomba, Queensland 4352, AUSTRALIA.

†Department of Mathematics and Computing, University of Southern Queensland, Toowoomba, Queensland 4352, AUSTRALIA.  
<http://www.sci.usq.edu.au/staff/aroberts>

AMS Subj Class: 37M99, 37L65, 65M20

## Contents

<b>1</b>	<b>Introduction</b>	<b>3</b>
<b>2</b>	<b>Use a homotopy in the inter-element coupling</b>	<b>5</b>
2.1	Introduce internal boundaries between elements . . . . .	6
2.2	Centre manifold theory supports the discretisation . . . . .	8
2.3	Approximate the shape of the centre manifold . . . . .	10
<b>3</b>	<b>Various holistic models</b>	<b>12</b>
3.1	Some holistic discretisations . . . . .	12
3.2	Illustration of subgrid field enhances our view . . . . .	15
3.3	The holistic discretisations are consistent . . . . .	17
<b>4</b>	<b>Holistic models accurately give steady states</b>	<b>20</b>
4.1	Reference accurate steady states . . . . .	21
4.2	Holistic models are accurate on coarse grids . . . . .	22
4.2.1	Bifurcation diagrams show success . . . . .	22
4.2.2	Holistic models outperform centered differences . . . . .	25
4.2.3	Grid refinement improves accuracy . . . . .	26
4.3	Comparison to Galerkin approximations . . . . .	27
4.4	Coarse grids allow large time steps . . . . .	29
<b>5</b>	<b>Holistic models are accurate for time dependent phenomena</b>	<b>31</b>
5.1	Dynamics near the steady states are reproduced . . . . .	32
5.2	Extend the Hopf bifurcations . . . . .	34
5.3	Dynamics of periodic patterns without odd symmetry . . . . .	36
<b>6</b>	<b>Conclusion</b>	<b>40</b>
<b>A</b>	<b>Computer algebra derives the discretisation</b>	<b>41</b>

## 1 Introduction

The Kuramoto–Sivashinsky equation, here

$$\frac{\partial u}{\partial t} + 4\frac{\partial^4 u}{\partial x^4} + \alpha \left( u\frac{\partial u}{\partial x} + \frac{\partial^2 u}{\partial x^2} \right) = 0. \quad (1)$$

was introduced by Sivashinsky [31] as a model of instabilities on interfaces and flame fronts, and Kuramoto [16] as a model of phase turbulence in chemical oscillations. It receives considerable attention as a model of complex spatio-temporal dynamics [13, 21, 5, 12, e.g.]. In the form (1), with  $2\pi$  periodic boundary conditions,  $\alpha$  is a bifurcation parameter that depends upon the size of the typical pattern [30]. The Kuramoto–Sivashinsky equation includes the mechanisms of linear negative diffusion  $\alpha u_{xx}$ , high-order dissipation  $4u_{xxxx}$ , and nonlinear advection/steepening  $\alpha uu_x$ . The system (1) has strong dissipative dynamics arising from the fourth order dissipation. Many modes of this system decay rapidly because of this strong dissipation. Thus the dynamics are dominated by a relatively few large scale modes. We create and explore the macroscopic modelling of the Kuramoto–Sivashinsky dynamics using holistic discretisation as initiated by MacKenzie & Roberts [18].

We study the Kuramoto–Sivashinsky equation here for several reasons. Firstly, the PDE is fourth order and therefore, following the example of Burgers’ equation [25], provides a further test case for the application of the holistic approach to higher order dissipative PDEs. Secondly, the Kuramoto–Sivashinsky equation is analogous to the Navier–Stokes equations of fluid dynamics. Holmes, Lumley & Berkooz [12] argued that these analogies exist on two levels: in the energy source and dissipation terms of both dynamical systems; and in the reflection and translational symmetries of the Kuramoto–Sivashinsky equation and the spanwise symmetries of the Navier–Stokes equations in the boundary layer. This analogy between symmetries suggests the Fourier series and corresponding modal interactions are comparable for these two problems. Thirdly, Cross & Hohenberg [5] describes how the Kuramoto–Sivashinsky equation exhibits the complexities of weak turbulence or spatio-temporal chaos. The complex dynamics of the Kuramoto–Sivashinsky equation (1) is searching test of the performance of the holistic approach to coarse grained modelling of dynamical systems.

Approximate inertial manifolds and variants [11, 9, 10, 1, 14, e.g.] capture the long-term low dimensional behaviour of the Kuramoto–Sivashinsky

equation. Most constructions of approximate inertial manifolds are based upon nonlinear Galerkin methods [22, 20, 14, 10, e.g.]. Approximate inertial manifolds are generally constructed by finding *global* eigenfunctions of the linear dynamics. Our approach is similar to these methods in that we project onto natural solutions of the PDE, and performs nearly as well, see §4.3. But in contrast, the holistic approach undertaken here bases analysis upon the *local* dynamics within and between finite elements and thus we contend it will be more useful in applications; for example, it is readily adapted to the modelling of a wide variety of physical boundary conditions [27].

Our approach is to divide the spatial domain into disjoint finite elements (§2.1). Initially these finite elements are decoupled and so dissipation causes the solution to exponentially quickly become constant in each element. We then couple the elements together so that information is exchanged between elements—parameterised by a coupling parameter  $\gamma$  so that  $\gamma = 1$  recovers the original Kuramoto–Sivashinsky equation. The coupling drives the evolution of the field in each element. We solve the Kuramoto–Sivashinsky PDE within each element with the coupling and hence resolve subgrid scale dynamics. Centre manifold theory [3, 23, e.g.] then provides the rigorous support for holistic models as introduced by Roberts [25] for Burgers’ equation and discussed in §2.2.

A low order analysis, reported in §3.1, of the Kuramoto–Sivashinsky equation (1) favours the discretisation

$$\begin{aligned} & \frac{du_j}{dt} + \frac{4u_{j+2} - 16u_{j+1} + 24u_j - 16u_{j-1} + 4u_{j-2}}{h^4} \\ & + \alpha \left( \frac{-u_{j+2} + 16u_{j+1} - 30u_j + 16u_{j-1} - u_{j-2}}{12h^2} \right) \\ & + \alpha \left( u_j \frac{u_{j+1} - u_{j-1}}{4h} + \frac{u_{j+1}^2 - u_{j-1}^2}{4h} - \frac{u_{j+2}u_{j+1} - u_{j-2}u_{j-1}}{12h} \right) \approx 0, \end{aligned} \quad (2)$$

where the  $u_j$ s are grid values spaced  $h$  apart. The first two lines of the holistic discretisation (2) shows the holistic method generates conventional centered finite difference approximations for the linear terms  $4u_{xxxx}$  and  $\alpha u_{xx}$ . The third line details a specific nonstandard approximation for the nonlinear term  $\alpha uu_x$ : it is a mix of three valid approximations to  $uu_x$ ; the specific mix is determined by the subgrid scale modelling of physical processes in the holistic approach, see §3.2. The holistic discretisation is not constructed by discretising the Kuramoto–Sivashinsky equation (1) term by term, rather the subgrid scale dynamics of (1) together with inter-element coupling generate the specific holistic discretisation (2).

The discretisation (2) is a low-order approximation. Centre manifold theory provides systematic refinements. Analysis to higher orders in nonlinearity or inter-element interaction, discussed in §3, gives further refinement to the discretisation. The higher order terms come from resolving more subgrid scale interactions. These higher order analyses lead to higher order consistency, as element size  $h \rightarrow 0$ , between the equivalent PDEs of the holistic discretisations, such as (2), and the Kuramoto–Sivashinsky PDE (see §3.3). Such consistency is further justification for our approach.

The bulk of this paper is then a comprehensive comparative study of the various models of the Kuramoto–Sivashinsky dynamics; further details are reported by MacKenzie [19]. A detailed numerical study of the holistic predictions for the steady states of the Kuramoto–Sivashinsky equation is the focal point of Section 4, followed by an exploration of the holistic predictions for the time dependent phenomena of the Kuramoto–Sivashinsky equation in Section 5. We look at: the predicted steady states, their stability and compare bifurcation diagrams; the dynamics near the steady states; Hopf bifurcations leading to period doubling sequences; and the spatio-temporal patterns at relatively large nonlinearity parameter  $\alpha$ . We find that the holistic models have excellent performance on coarse grids thus leading to simulations that may use large time steps. The excellent performance detailed herein is further evidence that the holistic approach is a robust and useful method for discretising PDEs.

## 2 Use a homotopy in the inter-element coupling

The construction of a discretisation is based upon breaking the spatial domain into disjoint finite elements and then joining them together again. We control this process by a coupling parameter  $\gamma$  that smoothly parametrises the transition between decoupled elements and fully coupled elements for which we recover a model for the original PDE. Furthermore, we construct the model using solutions of the PDE within each element and hence resolve subgrid scale dynamics. Centre manifold theory [3, 23, e.g.] provides the rigorous support for holistic models as introduced by Roberts [25] for Burgers' equation.

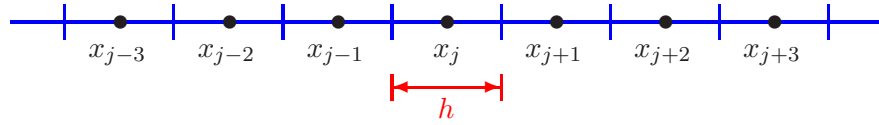


Figure 1: An example of the 1D grid with regular elements of width  $h$ . The  $j$ th element is centered about the grid point  $x_j$ . The vertical blue lines form the element boundaries, which for the  $j$ th element are located at  $x_{j\pm 1/2} = (j \pm 1/2)h$ .

## 2.1 Introduce internal boundaries between elements

Establish the spatial discretisation by dividing the domain into  $m$  elements of equal and finite width  $h$  and introducing an equispaced grid of collocation points,  $x_j = jh$ , at the centre of each element, see Figure 1.<sup>1</sup> Express the sub-grid field in the  $j$ th element by  $u = v_j(x, t)$  — we solve the Kuramoto–Sivashinsky PDE (1) with inter-element coupling introduced via artificial internal boundary conditions (IBCs). We introduce a homotopy in an inter-element coupling parameter  $\gamma$ : when  $\gamma = 0$  the elements are effectively isolated from each other, providing the basis for the application of centre manifold theory; whereas when evaluated at  $\gamma = 1$ , the elements are fully coupled together and hence the discretised model applies to the original PDE. Since the Kuramoto–Sivashinsky equation is fourth order we require four IBCs for each element to ensure satisfactory coupling between neighbouring elements. Here we use the non-local IBCs

$$\delta_x v_j(x, t) = \gamma \delta v_{j\pm 1/2}(x, t) \quad \text{at } x = x_{j\pm 1/2}, \quad (3)$$

$$\delta_x^3 v_j(x, t) = \gamma^2 \delta^3 v_{j\pm 1/2}(x, t) \quad \text{at } x = x_{j\pm 1/2}, \quad (4)$$

which are an extension of the non-local IBCs explored by Roberts [26] for Burgers' equation; a local possibility for the IBCs was explored by MacKenzie [19]. These non-local IBCs involve the centered difference operators  $\delta$  and  $\delta_x$ : the operator  $\delta_x$  denotes a centered difference in  $x$  only, with step  $h$ ; whereas the operator  $\delta$  denotes a centered difference applied to the grid index  $j$  with step 1; so for example, the first IBCs (3) is

$$v_j(x_{j\pm 1}, t) - v_j(x_j, t) = \gamma [v_{j\pm 1}(x_{j\pm 1}, t) - v_j(x_j, t)]. \quad (5)$$

Note: the field  $v_j(x, t)$  extends analytically to at least  $x_{j\pm 2}$ , to allow the application of the non-local IBCs (4). The physical interpretation of these IBCs is

<sup>1</sup>In principle, elements may be of unequal size. However, to simplify the analysis, herein all elements will be of equal width  $h$ .

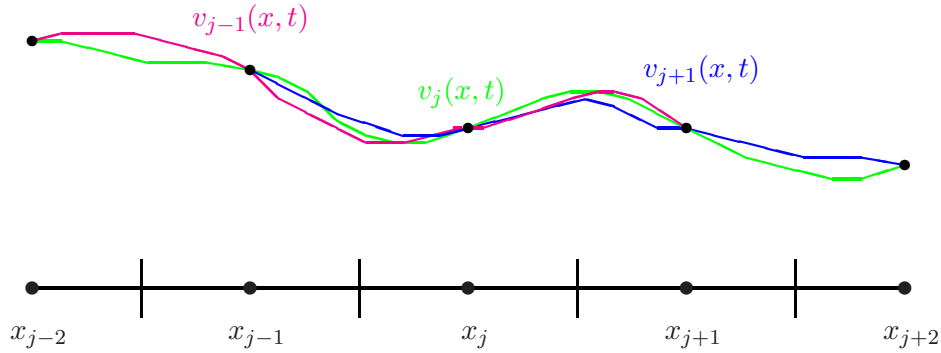


Figure 2: Schematic diagram of the fields  $v_j(x, t)$ ,  $v_{j+1}(x, t)$  and  $v_{j-1}(x, t)$  for the non-local IBCs (3–4) with  $\gamma = 1$ . See the fields pass through neighbouring grid values  $u_j$  and  $u_{j\pm 1}$ , and also  $u_{j\pm 2}$  when appropriate.

not obvious. Firstly, when  $\gamma = 0$ , (3–4) ensures the first and third differences in  $x$  of the field  $v_j$  centered about the element boundaries  $x_{j\pm 1/2}$  are zero. These isolate each element from its neighbours as there is then no coupling between them. In each element  $v_j(x, t) = \text{constant}$  is an equilibrium. It is dynamically attractive provided the instability controlled by  $\alpha/h^2$  is not too large compared with the dissipation of order  $1/h^4$ . This simple class of piecewise constant solutions provide the basis for analysing the  $\gamma \neq 0$  case when the elements are coupled together. Secondly, the non-local IBCs evaluated at  $\gamma = 1$  requires that the field  $v_j(x, t)$ , when extrapolated to  $x_{j\pm 1}$  and  $x_{j\pm 2}$ , is to equal the grid point value of the subgrid field of that element,  $u_{j\pm 1}$  and  $u_{j\pm 2}$  respectively. See the schematic representation in Figure 2 of these non-local boundary conditions evaluated at  $\gamma = 1$ . This restores sufficient continuity to ensure the holistic model applies to the original PDE.

The inter-element coupling parameter  $\gamma$  controls the flow of information between neighbouring elements. We construct solutions as power series expansions in the coupling parameter  $\gamma$ .<sup>2</sup> When  $\mathcal{O}(\gamma^2)$  terms are neglected in the holistic model, the field in the  $j$ th element involves information about the fields in the  $j \pm 1$  elements. Similarly, when  $\mathcal{O}(\gamma^3)$  terms are neglected in the approximation, the field in the  $j$ th element involves information about the fields in the  $j \pm 1$  and  $j \pm 2$  elements. Consequently, the order of  $\gamma$  retained in the holistic model controls the stencil width of the discretisation.

<sup>2</sup>Such homotopies are used successfully in other numerical methods. For example, Liao [17] proposed a homotopy in his general boundary element method from auxiliary linear operators whose fundamental solutions are well known. In our application the homotopy is only in the IBCs.

Roberts [26] argued that this particular form of the non-local IBCs ensure that these holistic models are consistent with any given PDE to high orders in the grid size  $h$  as  $h \rightarrow 0$ .

## 2.2 Centre manifold theory supports the discretisation

The existence, relevance and approximation theorems [3, 4, e.g.] of centre manifold theory apply to the Kuramoto–Sivashinsky PDE (1) with IBCs (3–4). Similar to the application to Burgers’ equation by Roberts [25], the result here is support for a low dimensional discrete model for the Kuramoto–Sivashinsky dynamics at finite grid size.

Theoretical support is based upon the piecewise constant solutions obtained when all the elements are insulated from each other. Adjoin to the Kuramoto–Sivashinsky PDE (1) the dynamically trivial equations for the coupling parameter  $\gamma$  and the nonlinearity parameter  $\alpha$ ,

$$\frac{\partial \gamma}{\partial t} = \frac{\partial \alpha}{\partial t} = 0, \quad (6)$$

and consider the dynamics in the extended state space  $(u(x), \gamma, \alpha)$ . Adjoining such trivial equations for parameters is commonly used to unfold bifurcations [3, §1.5]. In this extended space there is a subspace of fixed points with  $u = \text{constant}$  in each element and  $\gamma = \alpha = 0$ . Linearizing the PDE and IBCs about each fixed point,  $u = \text{constant} + u'(x, t)$ , gives

$$\frac{\partial u'}{\partial t} = -\frac{\partial^4 u'}{\partial x^4}, \quad \text{such that} \quad \delta_x u'(x, t)|_{x=x_{j\pm 1/2}} = \delta_x^3 u'(x, t)|_{x=x_{j\pm 1/2}} = 0.$$

The  $n$ th linear eigenmode associated with each element is

$$\alpha = \gamma = 0, \quad u' \propto e^{\lambda_n t} \cos \left[ \frac{n\pi}{h}(x - x_{j-1/2}) \right], \quad (7)$$

for the non-local IBCs (3–4), where  $n = 0, 1, \dots$  and the eigenvalue  $\lambda_n = -n^4 \pi^4 / h^4$ . There are also the trivial modes  $\gamma = \text{const}$  and  $\alpha = \text{const}$ . Therefore, in a spatial domain of  $m$  elements there are  $m + 2$  zero eigenvalues: one associated with each of the  $m$  elements; and two from the trivial (6). All other eigenvalues are negative and  $\leq -\pi^4 / h^4$ . Thus, the existence theorem, see [4, p.281] or [32, p.96], guarantees that a  $m + 2$  dimensional centre manifold  $\mathcal{M}$  exists for the Kuramoto–Sivashinsky PDE (1) with the trivial (6) and IBCs (3–4).



We parametrise the  $m + 2$  dimensional centre manifold  $\mathcal{M}$  by the  $m + 2$  parameters  $\gamma$ ,  $\alpha$  and the grid values  $u_j$ .<sup>3</sup> Denote  $\mathbf{u}$  as the vector of the  $m$  grid values. Thus for some function  $v$  the centre manifold  $\mathcal{M}$  is

$$u(x, t) = v(x; \mathbf{u}, \gamma, \alpha). \quad (8)$$

Equivalently, we decompose the centre manifold field into that for each element:

$$u = v(x; \mathbf{u}, \gamma, \alpha) = \sum_j v_j(x; \mathbf{u}, \gamma, \alpha) \chi_j(x), \quad (9)$$

where the characteristic function  $\chi_j(x)$  is 1 when  $x_{j-1/2} < x < x_{j+1/2}$ , and 0 otherwise; view the centre manifold as the union of all states of the collection of subgrid fields  $v_j(x; \mathbf{u}, \gamma, \alpha)$  over the physical domain. The corresponding amplitude condition, that the field in each element has to pass through its grid value, is

$$u_j = v(x_j; \mathbf{u}, \gamma, \alpha). \quad (10)$$

The existence theorem [4] also asserts that on the centre manifold the grid values  $u_j$  evolve deterministically in time according to the system of ODEs

$$\dot{u}_j = du_j/dt = g_j(\mathbf{u}, \gamma, \alpha), \quad (11)$$

where  $g_j$  is the restriction of the Kuramoto–Sivashinsky PDE (1) with the trivial (6) and IBCs (3–4) to the centre manifold  $\mathcal{M}$ . It is this evolution (11) of the grid values that gives the holistic discretisation.

Note that the centre manifold  $\mathcal{M}$  is global in  $u$  but local in  $\gamma$  and  $\alpha$ . When the parameters  $\gamma = \alpha = 0$  the Kuramoto–Sivashinsky PDE has a  $m$  dimensional “centre” subspace  $\mathcal{E}$  of fixed points with the field  $u$  being independently constant in each element; these are fixed points for all  $\mathbf{u}$ . When the parameters  $\gamma$  and  $\alpha$  are non-zero this subspace is “bent” to the curved centre manifold  $\mathcal{M}$ . Thus the models we construct are valid for small enough  $\gamma$  and  $\alpha$ , although we use them at finite  $\gamma$  and  $\alpha$ , but are formally valid for all  $|\mathbf{u}|$ . Numerical solutions of the centre manifold models, such as those in §3.2, indicate that parameter values as large as  $\gamma = 1$  and  $\alpha = 20$ –50 are indeed within the range of validity of our approach, even on relatively coarse grids.

We now support the claim that the evolution of the discrete grid values (11) actually models the Kuramoto–Sivashinsky system (1). The relevance theorem of centre manifolds, [4, p.282] or [32, p.128], guarantees that all

---

<sup>3</sup>These grid values are one choice for the measure of the field  $u$  in each element. Other choices are possible, but the grid values appear most convenient.

solutions of the Kuramoto–Sivashinsky system (1) with (6) and the IBCs (3–4), which remain in some neighbourhood of the subspace  $\mathcal{E}$  in  $(u(x), \gamma, \alpha)$  space are exponentially quickly attracted to the centre manifold  $\mathcal{M}$  and thence to a solution of the  $m$  discrete ODEs (11). For our application of centre manifold theory to the holistic model we seek regimes where this neighbourhood includes  $\gamma = 1$  and  $\alpha$  of interest. We estimate the rate of attraction by the leading negative eigenvalue, here  $\lambda_1 = -\pi^4/h^4$ . The actual rate of attraction may be less due to the difference between centre manifold  $\mathcal{M}$  and centre subspace  $\mathcal{E}$ , but  $\lambda_1$  will be the correct order of magnitude. This ensures the so-called asymptotic completeness [29]: after the exponentially quick transients of the approach to  $\mathcal{M}$  by any trajectory, the evolution of the discretisation (11) on  $\mathcal{M}$  accurately models the Kuramoto–Sivashinsky PDE (1).

### 2.3 Approximate the shape of the centre manifold

Having established that we may find a low dimensional description (8–11) of the interacting elements that is relevant to the Kuramoto–Sivashinsky system (1), we need to construct the shape of centre manifold and the corresponding evolution on the manifold.

The approximation theorem of Carr & Muncaster [4, p.283] assures us that upon substituting the ansatz (8–11) into the complete system and solving to some order of error in  $\alpha$  and  $\gamma$ , then  $\mathcal{M}$  and the evolution thereon will be approximated to the same order. However, we need to evaluate the approximations at the coupling parameter  $\gamma = 1$  because it is only then that the artificial internal boundaries are removed. Thus the actual error of the model due to the evaluation at  $\gamma = 1$  is not estimated. However, the holistic method for discretising the Kuramoto–Sivashinsky equation is supported three ways: firstly, the smooth homotopy from  $\gamma = 0$  with large spectral gap to the gravest decaying mode with decay rate  $\approx -\pi^4/h^4$ ; secondly the holistic models are consistent with the Kuramoto–Sivashinsky PDE to high order in grid size  $h$ , see §3.3; thirdly, we see in Sections 4–5 the holistic models model accurately both steady state solutions and time dependent phenomena of the Kuramoto–Sivashinsky system.

To construct the centre manifold, we solve for the field  $v_j$  in each element. For definiteness, here we consider domains periodic in space, or equivalently elements far from the influence of any physical boundary. By translational symmetry of the Kuramoto–Sivashinsky PDE (1) the subgrid field in each element is identical, except for the appropriate shift in the grid index  $j$ .

Thus, we construct the subgrid field and evolution for a general  $j$ th element, see some examples in Section 3

The algebraic details of the derivation of the centre manifold model (8–11) are handled by computer algebra. In an algorithm introduced by Roberts [24], iteration drives to zero the residuals of the governing PDE (1) and its IBCs (3–4) and amplitude condition (10). Since the algebraic details of the construction are tedious, they are not given; instead see the computer algebra procedure of [28].

This computer algebra is based upon driving the residuals of the governing equations to zero in the following manner. Recall from §2.2 that the centre manifold (8) is parametrised by the grid values  $\mathbf{u}$  and that the evolution of the grid values is given by (11). Thus substitute these into the Kuramoto–Sivashinsky PDE (1) and seek to solve

$$\frac{\partial v_j}{\partial t} = \sum_k \frac{\partial v_j}{\partial u_k} g_k = -4 \frac{\partial^4 v_j}{\partial x^4} - \alpha \left( \frac{\partial^2 v_j}{\partial x^2} + v_j \frac{\partial v_j}{\partial x} \right), \quad (12)$$

together with the non-local IBCs (3–4) and the amplitude equation (10), to some order in parameters  $\gamma$  and  $\alpha$ . The iteration is that given any approximation, denoted by  $\tilde{\phantom{v}}$ , we seek corrections, denoted by primes, such that  $v_j = \tilde{v}_j + v'_j$  and  $g_j = \tilde{g}_j + g'_j$ , better satisfy the Kuramoto–Sivashinsky PDE. Thus in each iteration we solve a problem of the form,

$$-4 \frac{\partial^4 v'_j}{\partial x^4} = g'_j + \text{Residual}, \quad (13)$$

where

$$\text{Residual} = \sum_k \frac{\partial \tilde{v}_j}{\partial u_k} g_k + 4 \frac{\partial^4 \tilde{v}_j}{\partial x^4} + \alpha \left( \frac{\partial^2 \tilde{v}_j}{\partial x^2} + \tilde{v}_j \frac{\partial \tilde{v}_j}{\partial x} \right), \quad (14)$$

together with the IBCs, for the corrections, primed quantities, to the subgrid field and the evolution of the grid values. Note: the residual in (14) is the residual of the Kuramoto–Sivashinsky system for the current approximation. The iteration scheme starts with the linear solution in each element, namely  $v_j(x, \mathbf{u}, \gamma, \alpha) = u_j$  and  $g_j(\mathbf{u}, \gamma, \alpha) = 0$ . The iteration terminates when the residuals of the Kuramoto–Sivashinsky PDE (12), and the IBCs, are zero to some order in  $\gamma$  and  $\alpha$ . Then theory assures us that the subgrid field in each element and the evolution of the grid values are correct to the same order in  $\gamma$  and  $\alpha$ .

### 3 Various holistic models

Here we record holistic models of the Kuramoto–Sivashinsky PDE (1), to various orders in coupling parameter  $\gamma$ , governing the width of the numerical stencil, and in the nonlinearity parameter  $\alpha$ . For use the models need to be evaluated at  $\gamma = 1$  as then the non-local IBCs (3–4) ensure sufficient continuity in the solution field. We write the models in terms of the centered difference and mean operators,

$$\delta u_j = u_{j+1/2} - u_{j-1/2} \quad \text{and} \quad \mu u_j = (u_{j+1/2} + u_{j-1/2})/2,$$

respectively. The models are constructed using a REDUCE program adapted from [28]. We only present in detail here holistic models to errors  $\mathcal{O}(\alpha^2)$  as the level of complexity increases enormously with the order of  $\alpha$ .

#### 3.1 Some holistic discretisations

In order to represent the spatial fourth derivative in the Kuramoto–Sivashinsky equation, we need at least a 5 point stencil approximation. Thus we determine the interactions between at least next-nearest neighbouring elements by obtaining up to at least quadratic terms in the coupling parameter  $\gamma$ .

**The  $\mathcal{O}(\gamma^3, \alpha^2)$  holistic discretisation** is

$$\begin{aligned} \dot{u}_j = & -\frac{\gamma\alpha}{h^2}\delta^2 u_j - \frac{\gamma\alpha}{h}u_j\delta\mu u_j - \frac{4\gamma^2}{h^4}\delta^4 u_j + \frac{\gamma^2\alpha}{12h^2}\delta^4 u_j \\ & + \frac{\gamma^2\alpha}{12h}(2u_j\delta^3\mu u_j + \delta^2 u_j\delta^3\mu u_j + \delta^4 u_j\delta\mu u_j) \\ & + \mathcal{O}(\gamma^3, \alpha^2), \end{aligned} \quad (15)$$

for the non-local IBCs (3–4). This forms a basic 5 point stencil approximation, since the evolution  $\dot{u}_j$  involves just  $u_j$ ,  $u_{j\pm 1}$  and  $u_{j\pm 2}$ . The first line of (15), when evaluated at  $\gamma = 1$ , gives a 2nd order centered difference approximation for the hyperdiffusion term  $4u_{xxxx}$ , a 4th order centered difference approximation to the linear growth term  $\alpha u_{xx}$ , and a 2nd order centered difference approximation to the nonlinear advection term  $\alpha u u_x$ . The second line modifies the nonlinear discretisation to account for interaction with effects caused by the next-nearest neighbour elements.

The holistic discretisation (15) contains the approximation

$$u u_x|_{x_j} \approx \left( u_j \frac{u_{j+1} - u_{j-1}}{4h} + \frac{u_{j+1}^2 - u_{j-1}^2}{4h} - \frac{u_{j+2}u_{j+1} - u_{j-2}u_{j-1}}{12h} \right). \quad (16)$$

when evaluated at  $\gamma = 1$ . This is a  $1/2 : 1 : -1/2$  mix of the approximations

$$uu_x|_{x_j} \approx u_j \frac{u_{j+1} - u_{j-1}}{2h} \approx \frac{u_{j+1}^2 - u_{j-1}^2}{4h} \approx \frac{u_{j+2}u_{j+1} - u_{j-2}u_{j-1}}{6h}, \quad (17)$$

respectively. This particular nonstandard approximation (16) to the nonlinear term  $\alpha uu_x$ , arises due to the modelling of subgrid scale interactions between the Kuramoto–Sivashinsky equation and the inter-element coupling. Such nonstandard approximations generated through this approach can have robust numerical characteristics [26, §2].

**The  $\mathcal{O}(\gamma^4, \alpha^2)$  holistic discretisation** is

$$\begin{aligned} \dot{u}_j = & -\frac{\gamma\alpha}{h^2}\delta^2 u_j - \frac{\gamma\alpha}{h}u_j\delta\mu u_j - \frac{4\gamma^2}{h^4}\delta^4 u_j + \frac{\gamma^2\alpha}{12h^2}\delta^4 u_j \\ & + \frac{2\gamma^3}{3h^4}\delta^6 u_j - \frac{\gamma^3\alpha}{90h^2}\delta^6 u_j \\ & + \frac{\gamma^2\alpha}{12h}(2u_j\delta^3\mu u_j + \delta^2 u_j\delta^3\mu u_j + \delta^4 u_j\delta\mu u_j) \\ & - \frac{\gamma^3\alpha}{480h}(16u_j\delta^5\mu u_j + 30\delta^4 u_j\delta^3\mu u_j + 40\delta^2 u_j\delta^3\mu u_j \\ & + 40\delta^4 u_j\delta\mu u_j + 28\delta^2 u_j\delta^5\mu u_j + 14\delta^6 u_j\delta\mu u_j \\ & + 7\delta^4 u_j\delta^5\mu u_j + 7\delta^6 u_j\delta^3\mu u_j) + \mathcal{O}(\gamma^4, \alpha^2). \end{aligned} \quad (18)$$

This discretisation forms a 7 point stencil approximation, involving  $u_j, u_{j\pm 1}, u_{j\pm 2}$  and  $u_{j\pm 3}$ . The first two lines of (18), when evaluated at  $\gamma = 1$ , give a 4th order centered difference approximation to the hyperdiffusion term, a 6th order centered difference approximation to the linear growth term, and a 2nd order centered difference approximation to the nonlinear advection term. The third and remaining lines account for higher order subgrid scale dynamics of the nonlinearity and its inter-element coupling to generate a 4th order centered difference approximation to the nonlinearity  $uu_x$ .

**The  $\mathcal{O}(\gamma^5, \alpha^2)$  holistic discretisation** is

$$\begin{aligned} \dot{u}_j = & -\frac{\gamma\alpha}{h^2}\delta^2 u_j - \frac{\gamma\alpha}{h}u_j\delta\mu u_j - \frac{4\gamma^2}{h^4}\delta^4 u_j + \frac{\gamma^2\alpha}{12h^2}\delta^4 u_j \\ & + \frac{2\gamma^3}{3h^4}\delta^6 u_j - \frac{\gamma^3\alpha}{90h^2}\delta^6 u_j \\ & - \frac{7\gamma^4}{60h^4}\delta^8 u_j + \frac{\gamma^4\alpha}{560h^2}\delta^8 u_j \end{aligned}$$

$$\begin{aligned}
& + \frac{\gamma^2 \alpha}{12h} (2u_j \delta^3 \mu u_j + \delta^2 u_j \delta^3 \mu u_j + \delta^4 u_j \delta \mu u_j) \\
& - \frac{\gamma^3 \alpha}{480h} (16 u_j \delta^5 \mu u_j + 30 \delta^4 u_j \delta^3 \mu u_j + 40 \delta^2 u_j \delta^3 \mu u_j \\
& \quad + 40 \delta^4 u_j \delta \mu u_j + 28 \delta^2 u_j \delta^5 \mu u_j + 14 \delta^6 u_j \delta \mu u_j \\
& \quad + 7 \delta^4 u_j \delta^5 \mu u_j + 7 \delta^6 u_j \delta^3 \mu u_j) \\
& + \frac{\gamma^4 \alpha}{60480h} (432 u_j \delta^7 \mu u_j + 3528 \delta^2 u_j \delta^5 \mu u_j + 1507 \delta^2 u_j \delta^7 \mu u_j \\
& \quad + 3780 \delta^4 u_j \delta^3 \mu u_j + 3951 \delta^4 u_j \delta^5 \mu u_j + 984 \delta^4 u_j \delta^7 \mu u_j \\
& \quad + 1764 \delta^6 u_j \delta \mu u_j + 3419 \delta^6 u_j \delta^3 \mu u_j + 1414 \delta^6 u_j \delta^5 \mu u_j \\
& \quad + 164 \delta^6 u_j \delta^7 \mu u_j + 523 \delta^8 u_j \delta \mu u_j + 656 \delta^8 u_j \delta^3 \mu u_j \\
& \quad + 164 \delta^8 u_j \delta^5 \mu u_j) + \mathcal{O}(\gamma^5, \alpha^2) . \tag{19}
\end{aligned}$$

This forms a 9 point stencil approximation, involving only  $u_j$ ,  $u_{j\pm 1}$ ,  $u_{j\pm 2}$ ,  $u_{j\pm 3}$  and  $u_{j\pm 4}$ . The first two lines of (19) when evaluated at  $\gamma = 1$  give a 6th order centered difference approximation for the hyperdiffusion term, an 8th order centered difference approximation for the linear growth term and a 2nd order centered difference approximation for the nonlinear advection term. The third and remaining lines provide modifications to model the nonlinear  $uu_x$  to 6th order through resolving subgrid scale dynamics.

We do not code these discretisations manually. Instead, the computer algebra program at [28] is used with the UNIX editor `sed` to automatically write the discretisation in a form suitable to be input to MATLAB for numerical exploration.

**Compare to conventional centered difference models.** Traditional direct finite differences generate the following approximations to the Kuramoto–Sivashinsky PDE (1):

- 5 point,

$$\dot{u}_j = -\frac{\alpha}{h} u_j \delta \mu u_j - \frac{\alpha}{h^2} \delta^2 u_j - \frac{4}{h^4} \delta^4 u_j + \mathcal{O}(h^2) ; \tag{20}$$

- 7 point,

$$\begin{aligned}
\dot{u}_j = & -\frac{\alpha}{h} \left( u_j \delta \mu u_j - \frac{1}{6} u_j \delta^3 \mu u_j \right) - \frac{\alpha}{h^2} \left( \delta^2 u_j - \frac{1}{12} \delta^4 u_j \right) \\
& - \frac{4}{h^4} \left( \delta^4 u_j - \frac{1}{6} \delta^6 u_j \right) + \mathcal{O}(h^4) ; \tag{21}
\end{aligned}$$

- 9 point,

$$\begin{aligned}
\dot{u}_j = & -\frac{\alpha}{h} \left( u_j \delta \mu u_j - \frac{1}{6} u_j \delta^3 \mu u_j + \frac{1}{30} u_j \delta^5 \mu u_j \right) \\
& - \frac{\alpha}{h^2} \left( \delta^2 u_j - \frac{1}{12} \delta^4 u_j + \frac{1}{90} \delta^6 u_j \right) \\
& - \frac{4}{h^4} \left( \delta^4 u_j - \frac{1}{6} \delta^6 u_j + \frac{7}{240} \delta^6 u_j \right) + \mathcal{O}(h^6) . \quad (22)
\end{aligned}$$

Consider the different view of the errors for the discretisations: the centered difference approximations (20–22) are justified by consistency as grid size  $h \rightarrow 0$ ; whereas the holistic discretisations (15–19) are supported by centre manifold theory at finite grid size  $h$ . The errors in the centre manifold approach are due to the truncation of dependence in the inter-element coupling parameter  $\gamma$  and the nonlinearity parameter  $\alpha$ . However, as argued by Roberts [26] for linear systems and as demonstrated in §3.3, the particular choice of the IBCs (3–4) ensures that the holistic discretisations *are also consistent as  $h \rightarrow 0$*  with the Kuramoto–Sivashinsky PDE (1).

### 3.2 Illustration of subgrid field enhances our view

Recall the collection of subgrid fields (9) over the physical domain form a state on the centre manifold. Here we plot some example subgrid fields for various holistic models. In particular, we examine subgrid fields of the holistic models of steady states of the Kuramoto–Sivashinsky PDE (1) at nonlinear parameter  $\alpha = 20$  and  $\alpha = 50$ . This is intended to reinforce the link between the abstract centre manifold description of the dynamics and the physical subgrid fields for the low order holistic models. We compare the fields with the Lagrangian interpolation that underlies traditional finite differences. Recall that the key methodology difference is that the subgrid fields of the holistic models are constructed by actual solutions of the Kuramoto–Sivashinsky PDE, see §2.3.

We restrict attention to odd symmetric solutions that are  $2\pi$ -periodic. This is done to compare with the numerical investigations of Jolly [14] which we consider in more detail in Sections 4 and 5. Set a grid of 8 equi-spaced elements on the interval  $[0, \pi]$ . The subgrid fields are plotted for approximations to the steady states of the Kuramoto–Sivashinsky equation (1) with these periodic boundary conditions, computed using holistic discretisations at  $\alpha = 20$  and  $\alpha = 50$ .

Figure 3: Subgrid field (green curve) of the holistic model (15) and a Lagrangian interpolant (magenta curve) constructed through a 2nd order centered difference approximation for a steady state of the Kuramoto–Sivashinsky equation at  $\alpha = 20$ , with 8 elements on  $[0, \pi]$ . An accurate solution is also plotted in blue.

Figure 4: Subgrid fields of the holistic models with errors  $\mathcal{O}(\gamma^3, \alpha^2)$  (15) (green),  $\mathcal{O}(\gamma^4, \alpha^2)$  (18) (olive green) and  $\mathcal{O}(\gamma^5, \alpha^2)$  (19) (cyan), for a steady state of the Kuramoto–Sivashinsky equation at  $\alpha = 20$ , with 8 elements on  $[0, \pi]$ . An accurate solution is also plotted in blue.

Figure 3 displays an accurate solution (blue curve) of the Kuramoto–Sivashinsky PDE to compare with the subgrid field (green curve) of the 5 point stencil  $\mathcal{O}(\gamma^3, \alpha^2)$  holistic approximation (15) (green discs), and the Lagrangian interpolant (magenta curve) constructed through a 2nd order centered difference approximation (magenta discs), for a steady state at  $\alpha = 20$ . Observe the collection of subgrid fields forms the field  $u$  which is a state on the centre manifold. The subgrid field of the holistic model more accurately represents the steady state of the Kuramoto–Sivashinsky equation at  $\alpha = 20$ , on this coarse grid.

Higher order holistic models improve the accuracy and continuity of the subgrid field. Figure 4 displays the subgrid fields of three holistic models for the same steady state of the Kuramoto–Sivashinsky PDE depicted in Figure 3 for  $\alpha = 20$ . The  $\mathcal{O}(\gamma^3, \alpha^2)$  holistic model (15) (green) is the least accurate and has the largest jump at element boundaries. The  $\mathcal{O}(\gamma^4, \alpha^2)$  (18) model (olive green) displays improvement over the holistic  $\mathcal{O}(\gamma^3, \alpha^2)$  approximation. The  $\mathcal{O}(\gamma^5, \alpha^2)$  (19) model (cyan) is the most accurate, being almost indistinguishable from the correct curve.

Figure 5 shows a steady state of the Kuramoto–Sivashinsky PDE at  $\alpha = 50$ . The accurate field is symmetric (blue curve). For this value of the nonlinearity there is no steady state solution for centered difference approximations of either 2nd (20), 4th (21) or 6th order (22) on this coarse grid of 8 elements on  $[0, \pi]$ . However, the 5 point stencil holistic approximation with errors

Figure 5: Subgrid fields of the holistic models with errors  $\mathcal{O}(\gamma^3, \alpha^2)$  (15) (green),  $\mathcal{O}(\gamma^4, \alpha^2)$  (18) (olive green) and  $\mathcal{O}(\gamma^5, \alpha^2)$  (19) (cyan), for a steady state of the Kuramoto–Sivashinsky equation at  $\alpha = 50$ , with 8 elements on  $[0, \pi]$ . An accurate solution is also plotted in blue.



$\mathcal{O}(\gamma^3, \alpha^2)$  (15) (green) models this steady state of the Kuramoto–Sivashinsky equation even for such a large value of the nonlinearity on this coarse grid. This  $\mathcal{O}(\gamma^3, \alpha^2)$  holistic solution has significant jumps across the subgrid field at element boundaries; moreover, the subgrid field is not symmetric and is most inaccurate near the centre of the spatial domain considered here. The 7 point stencil holistic approximation with errors  $\mathcal{O}(\gamma^4, \alpha^2)$  (18) (olive green) is more accurate with smaller jumps between neighbouring the subgrid fields, but is also not symmetric. The 9 point stencil holistic approximation with errors  $\mathcal{O}(\gamma^5, \alpha^2)$  (19) (cyan) is the most accurate of the holistic models illustrated here; it is symmetric and the jumps between neighbouring subgrid fields are almost indiscernible.

These illustrations of the subgrid fields of steady states of the Kuramoto–Sivashinsky equation at  $\alpha = 20$  and  $\alpha = 50$  indicate the holistic models perform well even at such large values of a supposedly small parameter. The performance of the holistic models are explored further in Section 4 for steady states and Section 5 for time dependent phenomena.

### 3.3 The holistic discretisations are consistent

Holistic models constructed by implementing the IBCs (3–4) have dual justification [26]: they are supported by centre manifold theory for small enough  $\alpha$  and  $\gamma$ ; as well as being justified by their consistency as the grid size  $h \rightarrow 0$ . We explore consistency as a well established feature of numerical analysis.<sup>4</sup>

Here we examine the equivalent PDEs for the holistic discretisations (15–19) evaluated at  $\gamma = 1$ , and the centered difference approximations (20–22). These equivalent PDEs establish the  $\mathcal{O}(h^{2p-2})$  consistency with the Kuramoto–Sivashinsky PDE for holistic models constructed with residuals  $\mathcal{O}(\gamma^{p+1})$ .

Roberts [26] proved that using IBCs of the form introduced in §2 and retaining terms up to  $\gamma^p$  in the holistic approximations results in approximations which are consistent with the *linear* terms of the Kuramoto–Sivashinsky equation (1) to  $\mathcal{O}(h^{2p-2})$ , provided  $p \geq 2$ . However, it appears that using the IBCs (3–4) also ensures  $\mathcal{O}(h^{2p-2})$  consistency for the nonlinear terms. As yet no formal proof exists of this nonlinear consistency, but all holistic models of the Kuramoto–Sivashinsky equation, containing terms up to  $\gamma^7$  and  $\alpha^4$  and constructed using (3–4) are nonlinearly consistent (although not all are recorded here).

---

<sup>4</sup>But note that high order consistency is not a primary goal of this holistic approach, since we aim to develop and support models for finite element size  $h$ .

Find the equivalent PDEs for the various discretisations by expanding the discretisations in grid size  $h$  about a grid point  $x_j$ . That is, write

$$u_{j\pm m} = u_j \pm mh \frac{\partial u_j}{\partial x} + m^2 \frac{h^2}{2} \frac{\partial^2 u_j}{\partial x^2} + \sum_{k=3}^{\infty} (\pm m)^k \frac{h^k}{k!} \frac{\partial^k u_j}{\partial x^k}, \quad (23)$$

to whatever order in  $h$  is required. Computer algebra performs the tedious details.

**The equivalent PDE for the 5 point holistic discretisation** (15), which retain terms up to  $\gamma^2$ , is

$$\begin{aligned} \frac{\partial u}{\partial t} = & -\alpha \left( u \frac{\partial u}{\partial x} + \frac{\partial^2 u}{\partial x^2} \right) - 4 \frac{\partial^4 u}{\partial x^4} - \frac{2h^2}{3} \frac{\partial^6 u}{\partial x^6} + \frac{h^4}{20} \frac{\partial^8 u}{\partial x^8} \\ & + \alpha h^4 \left( \frac{1}{48} \frac{\partial^3 u}{\partial x^3} \frac{\partial^2 u}{\partial x^2} + \frac{1}{48} \frac{\partial^4 u}{\partial x^4} \frac{\partial u}{\partial x} + \frac{1}{30} u \frac{\partial^5 u}{\partial x^5} + \frac{1}{90} \frac{\partial^6 u}{\partial x^6} \right) \\ & + \mathcal{O}(h^6). \end{aligned} \quad (24)$$

The equivalent PDE for the 5 point centered difference approximation (20) is

$$\begin{aligned} \frac{\partial u}{\partial t} = & -\alpha \left( u \frac{\partial u}{\partial x} + \frac{\partial^2 u}{\partial x^2} \right) - 4 \frac{\partial^2 u}{\partial x^2} \\ & - h^2 \left( \alpha \frac{1}{6} \frac{\partial^3 u}{\partial x^3} \frac{\partial u}{\partial x} + \alpha \frac{1}{12} \frac{\partial^4 u}{\partial x^4} + \frac{2}{3} \frac{\partial^6 u}{\partial x^6} \right) \\ & + \mathcal{O}(h^4). \end{aligned} \quad (25)$$

Observe that both equivalent PDEs (24–25) are  $\mathcal{O}(h^2)$  accurate. The coefficients of the error terms are different in both of these equivalent PDEs, with those of (15) having fewer error terms.

**The equivalent PDE for the 7 point holistic discretisation** (18), which retains terms up to  $\gamma^3$ , is

$$\begin{aligned} \frac{\partial u}{\partial t} = & -\alpha \left( u \frac{\partial u}{\partial x} + \frac{\partial^2 u}{\partial x^2} \right) - 4 \frac{\partial^4 u}{\partial x^4} - \frac{7h^4}{60} \frac{\partial^8 u}{\partial x^8} + \frac{13h^6}{756} \frac{\partial^{10} u}{\partial x^{10}} \\ & - \alpha h^6 \left( \frac{17}{640} \frac{\partial^4 u}{\partial x^4} \frac{\partial^3 u}{\partial x^3} + \frac{7}{384} \frac{\partial^5 u}{\partial x^5} \frac{\partial^2 u}{\partial x^2} + \frac{3}{320} \frac{\partial^6 u}{\partial x^6} \frac{\partial u}{\partial x} \right) \\ & + \frac{1}{140} u \frac{\partial^7 u}{\partial x^7} + \frac{1}{560} \frac{\partial^8 u}{\partial x^8} \\ & + \mathcal{O}(h^8). \end{aligned} \quad (26)$$

Whereas the equivalent PDE for the 7 point centered difference approximation (21) is

$$\begin{aligned} \frac{\partial u}{\partial t} = & -\alpha \left( u \frac{\partial u}{\partial x} + \frac{\partial^2 u}{\partial x^2} \right) - 4 \frac{\partial^2 u}{\partial x^2} \\ & - h^4 \left( \alpha \frac{1}{30} \frac{\partial^5 u}{\partial x^5} \frac{\partial u}{\partial x} + \alpha \frac{1}{90} \frac{\partial^6 u}{\partial x^6} + \frac{7}{60} \frac{\partial^8 u}{\partial x^8} \right) \\ & + \mathcal{O}(h^6). \end{aligned} \quad (27)$$

The two equivalent PDEs (26–27) are  $\mathcal{O}(h^4)$  accurate, and again the holistic discretisation has fewer errors.

**The equivalent PDEs for the 9 point holistic discretisation** (18), which retain terms up to  $\gamma^4$ , is

$$\begin{aligned} \frac{\partial u}{\partial t} = & -\alpha \left( u \frac{\partial u}{\partial x} + \frac{\partial^2 u}{\partial x^2} \right) - 4 \frac{\partial^4 u}{\partial x^4} - \frac{41h^6}{1890} \frac{\partial^{10} u}{\partial x^{10}} + \frac{13h^8}{2700} \frac{\partial^{12} u}{\partial x^{12}} \\ & + \alpha h^8 \left( \frac{3433}{138240} \frac{\partial^5 u}{\partial x^5} \frac{\partial^4 u}{\partial x^4} + \frac{5927}{322560} \frac{\partial^6 u}{\partial x^6} \frac{\partial^3 u}{\partial x^3} + \frac{499}{53760} \frac{\partial^7 u}{\partial x^7} \frac{\partial^2 u}{\partial x^2} \right. \\ & \left. + \frac{29}{8960} \frac{\partial^8 u}{\partial x^8} \frac{\partial u}{\partial x} + \frac{1}{630} u \frac{\partial^9 u}{\partial x^9} + \frac{1}{3150} \frac{\partial^{10} u}{\partial x^{10}} \right) \\ & + \mathcal{O}(h^{10}). \end{aligned} \quad (28)$$

The equivalent PDE for the 9pt centered difference approximation (22) is

$$\begin{aligned} \frac{\partial u}{\partial t} = & -\alpha \left( u \frac{\partial u}{\partial x} + \frac{\partial^2 u}{\partial x^2} \right) - 4 \frac{\partial^2 u}{\partial x^2} \\ & - h^6 \left( \alpha \frac{1}{140} \frac{\partial^7 u}{\partial x^7} \frac{\partial u}{\partial x} + \alpha \frac{1}{560} \frac{\partial^8 u}{\partial x^8} + \frac{41}{1890} \frac{\partial^{10} u}{\partial x^{10}} \right) \\ & + \mathcal{O}(h^8). \end{aligned} \quad (29)$$

Again the the equivalent PDEs (28–29) are  $\mathcal{O}(h^6)$  accurate, with the holistic discretisation having fewer error terms.

Although there is no proof of nonlinear consistency in general, we have demonstrated it here for these three holistic discretisations, and have found nonlinear consistency for all models investigated.

Figure 6: Accurate bifurcation diagram  $0 \leq \alpha \leq 70$  for the Kuramoto–Sivashinsky equation, using a 6th order centered difference approximation with 48 points on the interval  $[0, \pi]$ . A signed  $L^2$  norm is plotted against  $\alpha$

## 4 Holistic models accurately give steady states

The relevance of our holistic models is rigorously supported by centre manifold theory for sufficiently small parameters  $\gamma$  and  $\alpha$ . However, the holistic models must be evaluated at coupling parameter  $\gamma = 1$  to model the dynamics of the Kuramoto–Sivashinsky equation. The important question: Does evaluating the holistic models at  $\gamma = 1$  provide useful and accurate numerical models? Numerical experiments detailed in this and the next section provide strong support that it does.

In this section we explore the accuracy of the holistic models by constructing and comparing bifurcation diagrams of the various holistic discretisations to conventional explicit centered difference approximations and to the bifurcation diagrams presented by Jolly et al. [14] for various traditional Galerkin and nonlinear Galerkin approximations.

We restrict exploration to solutions that are both  $2\pi$  periodic and odd: thus

$$u(x, t) = u(x + 2\pi, t) \quad \text{and} \quad u(x, t) = -u(2\pi - x, t). \quad (30)$$

We also restrict the nonlinearity parameter to the range  $0 \leq \alpha \leq 70$ . These restrictions are to compare our results to those of Jolly et al. [14] for approximate inertial manifold methods. For this range of nonlinearity  $\alpha$  the trivial solution  $u = 0$  undergoes pitchfork bifurcations at  $\alpha = 4, 16, 36, 64$  leading to the unimodal, bimodal, trimodal and quadrimodal branches respectively, see the bifurcation diagram Figure 6.

Such bifurcation diagrams usefully summarise qualitative and quantitative information for a large range of the nonlinearity parameter  $\alpha$ . We use the software package XPPAUT [8], which incorporates the continuation software AUTO [7], to calculate the bifurcation information. The information is then filtered through a function written in MATLAB to draw the bifurcation diagram. The input to XPPAUT is a text `.ode` file describing the set of ODEs. Because the holistic models contain a large number of terms the `.ode` files are generated automatically using REDUCE and MATLAB which also incorporates the odd periodic requirement (30), see [19] for more details.

Figure 7: Some examples of the stable equilibria of the Kuramoto–Sivashinsky equation. Dark blue curves are solutions along the negative unimodal and bimodal branches. Light blue curves are stable solutions along the negative trimodal branch.

#### 4.1 Reference accurate steady states

Here we introduce accurate solutions for the steady states of the Kuramoto–Sivashinsky equation (1) over the range  $0 \leq \alpha \leq 70$  as summarised in the bifurcation diagram of Figure 6. Accurate solutions are produced by a 6th order accurate centered difference approximation (22) with 48 grid points on the spatial interval  $[0, \pi]$ . These provide the reference for the approximations on coarse grids, and serve to also introduce the conventions we adopt in bifurcation diagrams.

For all the bifurcation diagrams a signed solution norm is plotted against the nonlinearity parameter  $\alpha$ . This is different to the convention adopted by Jolly et al. [14] but empowers us to investigate more detail by showing positive and negative branches—stability differs along these branches. For example, see in Figure 6 that the negative bimodal branch is stable for  $16.140 < \alpha < 22.556$ , whereas the positive bimodal branch is unstable. The solution norm is signed corresponding to the sign of the the first grid value,  $u_1 = u(x_1)$ . The blue curves are branches of stable fixed points and the red curves are branches of unstable fixed points. The open squares denote pitchfork bifurcations and the black squares denote Hopf bifurcations.

The labeling scheme used in Figure 6 follows that of Jolly et al. [14] and Scovel [30] with the addition of a plus or minus sign depending upon the sign of  $u_1$ . For example, the secondary bifurcation on the negative bimodal branch is labeled  $R_2b_1-$  from the labeling scheme of Scovel with the addition of the  $-$  sign because it occurs on the negative branch. Figure 6 appears to show several discontinuities. For example, the positive unimodal branch ends at approximately  $\alpha = 12$ . This apparent discontinuity arises due to the convention adopted here of taking the sign of  $u_1$  to sign the norm: actually there is a continuous transformation as the positive unimodal branch and the negative unimodal branch transform into the negative bimodal branch. It is straightforward to sign the branch near the trivial solution, but away from the trivial solution the distinction between positive and negative may be ambiguous and occasionally leads to jumps in the bifurcation diagram.

For later comparison see in Figure 7 some of the stable equilibria of the Kuramoto–Sivashinsky equation in the regime of interest,  $0 \leq \alpha \leq 70$ . Figures 7a,b,c show solutions on the negative unimodal branch at  $\alpha = 1, 5, 10$

Figure 8: Some accurate solutions plotted with holistic and centered difference approximations on coarse grids. Blue curves are accurate solutions, green curves are the holistic approximation with IBCs (3–4) with errors  $\mathcal{O}(\gamma^5, \alpha^2)$  on 8 elements. Magenta curves are a 6th order centered difference approximation with 8 grid points.

Figure 9: Bifurcation diagrams for coarse grid approximations with 8 elements on  $[0, \pi]$  for (a) holistic model  $\mathcal{O}(\gamma^5, \alpha^2)$ , (b) centered difference 6th order.

respectively. Figures 7d,e,f show solutions on the negative bimodal branch at  $\alpha = 20, 30, 40$  respectively. The dark blue curves in Figures 7g,h,i show solutions on the negative bimodal branch and the light blue curves are solutions on the negative trimodal branch at  $\alpha = 50, 55, 60$  respectively.

## 4.2 Holistic models are accurate on coarse grids

We begin investigating the performance of the holistic models by considering the  $\mathcal{O}(\gamma^5, \alpha^2)$  holistic model (19) (9 point stencil,  $\mathcal{O}(h^6)$  consistent). We investigate its reproduction of the steady states of the Kuramoto–Sivashinsky system using coarse grids on the interval  $[0, \pi]$ .

Figure 8 shows accurate solutions of the Kuramoto–Sivashinsky equation (1) with odd boundary conditions (30) in blue. The holistic model with errors  $\mathcal{O}(\gamma^5, \alpha^2)$  and 8 elements is shown in green: Figure 8g,h,i, the bottom row, shows that the holistic model with errors  $\mathcal{O}(\gamma^5, \alpha^2)$  gives at large non-linearity the stable bimodal and trimodal solutions,  $\alpha = 50$  and  $\alpha = 55$ , and the stable bimodal solution at  $\alpha = 60$ . Magenta curves are solutions of the 6th order centered difference approximation (22) with 8 grid points—it has equal stencil width to the holistic model. The 6th order centered difference approximation does not give any stable solutions for  $\alpha \geq 50$ . The holistic model provides reasonable solutions where comparable traditional methods do not.

### 4.2.1 Bifurcation diagrams show success

Now turn to the bifurcation diagram to obtain a more comprehensive view. We see the holistic model has good bifurcation diagrams on a coarse grid of 8 elements and even with just 6 elements.

Figure 10: Bifurcation diagrams for coarse grid approximations with 6 elements on  $[0, \pi]$  for (a) holistic model  $\mathcal{O}(\gamma^5, \alpha^2)$ , (b) centered difference 6th order.

Figure 9 shows a side by side comparison of the holistic model with errors  $\mathcal{O}(\gamma^5, \alpha^2)$  with 8 elements on  $[0, \pi]$  and the 6th order centered difference approximation with 8 grid points on  $[0, \pi]$ . These approximations are both 9 point stencil approximations. The accurate bifurcation diagram is also plotted in grey but without any stability information. The signed  $L_2$  norms for the bifurcation diagrams on the coarse grid of 8 elements are adjusted by a factor of  $\sqrt{6}$  to allow comparison to the accurate bifurcation diagram constructed with 48 grid points on  $[0, \pi]$ . Throughout this paper when comparing bifurcation diagrams of different grid resolutions, the signed  $L_2$  norms are adjusted this way to provide a consistent reference. Figure 9a shows the  $\mathcal{O}(\gamma^5, \alpha^2)$  holistic model gives good agreement with the accurate bifurcation diagram for  $\alpha < 40$  and qualitatively reproduces most of the bifurcation picture for  $40 < \alpha < 70$ . The  $\mathcal{O}(\gamma^5, \alpha^2)$  holistic model does not detect the bifurcation points  $R_3t_2 \pm$  on this coarse grid and the bifurcation points  $R_3t_1 \pm$  are incorrectly identified as fold points. However, the  $\mathcal{O}(\gamma^5, \alpha^2)$  holistic model finds all of the other bifurcation points in this range of  $\alpha$ . Figure 9b shows the 6th order centered difference approximation gives good agreement with the accurate bifurcation diagram only for  $\alpha < 20$  and qualitatively reproduces the bifurcation diagram for  $20 < \alpha < 40$ . The 6th order centered difference approximation performs poorly for  $\alpha > 40$ . Table 1 lists the values of  $\alpha$  at which the bifurcation points occur and confirms the  $\mathcal{O}(\gamma^5, \alpha^2)$  holistic model performs more accurately than the 6th order centered difference approximation on this coarse grid of 8 elements.

Figure 10 is a side by side comparison of the same  $\mathcal{O}(\gamma^5, \alpha^2)$  holistic model to the 6th order centered difference approximation, on an even coarser grid of just 6 elements. The superior performance of the holistic model is again evident. We conjecture that the superior performance of the holistic discretisation is due to its systematic modelling of the subgrid scale processes. These bifurcation diagrams, Figures 9 and 10, give excellent support to the holistic approach to generating approximations for the Kuramoto–Sivashinsky equation.

We also investigate various holistic models for the Kuramoto–Sivashinsky PDE by comparing bifurcation diagrams of holistic models of higher orders. We examine bifurcation diagrams for holistic models with errors  $\mathcal{O}(\gamma^p, \alpha^q)$ , for  $3 \leq p \leq 5$  and  $2 \leq q \leq 4$ , and find that retaining terms of higher order in coupling parameter  $\gamma$ , corresponding to wider stencil approximations, gives

Table 1:  $\alpha$  values at which bifurcation points occur for the various coarse grid approximations; \* denotes bifurcation point identified as fold point.

Approximation	$R_2b_1$	$R_2b_2$	$R_2b_3$	$R_2b_4$	$R_3t_1$	$R_3t_2$	$R_4b_1$	$R_4q_1$
Accurate 48 pts								
6th order	16.14	22.56	52.89	63.74	36.23	50.91	64.56	64.28
Holistic 8 elements								
$\mathcal{O}(\gamma^3, \alpha^2)$	14.64	20.36	39.34	44.96	29.28*	—	45.28	44.87
$\mathcal{O}(\gamma^3, \alpha^3)$	14.65	20.52	39.66	45.16	29.33*	—	45.47	44.96
$\mathcal{O}(\gamma^3, \alpha^4)$	14.65	20.53	39.72	45.21	29.33*	—	45.51	44.97
$\mathcal{O}(\gamma^4, \alpha^2)$	16.00	22.56	48.62	57.38	34.73*	—	57.89	57.49
$\mathcal{O}(\gamma^4, \alpha^3)$	16.00	22.56	48.25	56.84	34.73*	—	57.45	57.28
$\mathcal{O}(\gamma^4, \alpha^4)$	16.00	22.57	48.10	56.63	34.73*	—	57.30	57.21
$\mathcal{O}(\gamma^5, \alpha^2)$	16.13	22.72	51.54	61.54	35.89*	—	62.20	61.78
$\mathcal{O}(\gamma^5, \alpha^3)$	16.13	22.73	51.53	61.37	35.91*	—	62.04	61.70
$\mathcal{O}(\gamma^5, \alpha^4)$	16.13	22.73	51.60	61.38	35.91*	—	62.02	61.69
Centered 8 pts								
2nd order	15.30	19.81	—	—	—	—	—	—
4th order	16.02	21.55	—	—	35.94*	—	—	—
6th order	16.12	21.99	—	—	35.83*	—	—	—
Holistic 12 elements								
$\mathcal{O}(\gamma^3, \alpha^2)$	15.45	21.67	45.96	53.94	32.86	45.98	54.49	54.17
$\mathcal{O}(\gamma^3, \alpha^3)$	15.45	21.69	46.05	54.00	32.87	46.33	54.55	54.20
$\mathcal{O}(\gamma^4, \alpha^2)$	16.11	22.62	51.93	62.10	35.90	50.92	62.83	62.52
$\mathcal{O}(\gamma^4, \alpha^3)$	16.11	22.62	51.94	62.10	35.90	50.94	62.83	62.52
Centered 12 pts								
2nd order	15.77	21.68	48.33	57.63	34.36	44.70	58.34	58.36
4th order	16.12	22.37	51.74	62.33	35.98	48.62	63.11	62.98

much greater improvement in accuracy than retaining terms of higher order in the nonlinearity parameter  $\alpha$ .

Figure 11 shows the bifurcation diagrams for the holistic models up to and including the  $\mathcal{O}(\gamma^5, \alpha^4)$  holistic model. Surveying across the columns of Figure 11 see the bifurcation diagrams for holistic models of increasing order of coupling parameter  $\gamma$ , corresponding to approximations of increasing stencil width. For example, Figure 11a,b,c shows the bifurcation diagrams for the holistic models (15), (18) and (19) respectively. Surveying down the rows of Figure 11 see the bifurcation diagrams for increasing orders of the nonlinearity parameter  $\alpha$ . Figure 11 illustrates the improvement in accuracy

Figure 11: Bifurcation diagrams for the holistic models with 8 elements on the interval  $[0, \pi]$  up to and including the  $\mathcal{O}(\gamma^5, \alpha^4)$  holistic model.



of the higher order holistic models. Note first the dramatic improvement in accuracy gained by moving from left to right across Figure 11, corresponding to approximations of higher orders in the coupling parameter  $\gamma$ .

Second, see that less improvement is gained by moving from top to bottom of Figure 11, corresponding to approximations of higher order in the nonlinearity parameter  $\alpha$ . There are some peculiarities about this series of bifurcation pictures for holistic models of increasing order in  $\alpha$ . For the 5 point stencil approximations displayed in the first column of Figures 11, higher orders in  $\alpha$  appear to gain some improvement. In particular Figures 11d,g show the  $\mathcal{O}(\gamma^3, \alpha^3)$  and  $\mathcal{O}(\gamma^3, \alpha^4)$  holistic models reproduce the unstable trimodal branches that were missing from the  $\mathcal{O}(\gamma^3, \alpha^2)$  bifurcation diagram shown in Figure 11a. However, for the 7 point stencil approximations displayed in the second column of Figure 11, holistic models of higher orders in  $\alpha$  lose some features of the Kuramoto–Sivashinsky system. The correct behaviour of the unstable trimodal and quadrimodal branches is reproduced for the  $\mathcal{O}(\gamma^4, \alpha^2)$  model shown in Figure 11b, but not reproduced for the higher order  $\mathcal{O}(\gamma^4, \alpha^3)$  and  $\mathcal{O}(\gamma^4, \alpha^4)$  models shown in Figures 11e,h respectively. For the 9 point stencil approximations, displayed in the third column of Figures 11, the  $\mathcal{O}(\gamma^5, \alpha^2)$  holistic model shown in Figure 11c, reproduces the unstable trimodal branch whereas the higher order  $\mathcal{O}(\gamma^5, \alpha^3)$  model shown in Figure 11f, does not reproduce the unstable trimodal branch. These peculiarities suggest that while we have observed excellent performance of the holistic models constructed with the non-local IBCs on coarse grids, it may be possible that modifications could be made to the non-local IBCs such that higher order approximations in the nonlinear parameter are improved. Exploration of possible such modifications are left for further research.

#### 4.2.2 Holistic models outperform centered differences

In §4.2.1 we saw that the performance of the  $\mathcal{O}(\gamma^5, \alpha^2)$  holistic model (19) constructed with non-local IBCs was far superior to the explicit 6th order centered difference approximation (22). To complete the comparison of holistic models to explicit centered difference schemes, we compare the  $\mathcal{O}(\gamma^3, \alpha^2)$  (15) and  $\mathcal{O}(\gamma^4, \alpha^2)$  (18) holistic models to the 2nd order (20) and 4th order (21) centered difference approximations respectively; these are 5 point and 7 point discretisations respectively.

The first row of Figure 12 is a side by side comparison of the  $\mathcal{O}(\gamma^3, \alpha^2)$  holistic model and the 2nd order centered difference approximation with 8 elements on  $[0, \pi]$ . The second row of Figure 12 is a side by side comparison of

Figure 12: Bifurcation diagrams for (a)  $\mathcal{O}(\gamma^3, \alpha^2)$  holistic model, (b) 2nd order centered difference, (c)  $\mathcal{O}(\gamma^4, \alpha^2)$  holistic model and (d) 4th order centered difference all with 8 elements on the interval  $[0, \pi]$

Figure 13: Bifurcation diagrams for the holistic models with 12 elements on the interval  $[0, \pi]$ . Compare with Figure 11 with 8 elements.

the  $\mathcal{O}(\gamma^4, \alpha^2)$  holistic model and the 4th order centered difference approximation on the same coarse grid. The accurate bifurcation diagram is plotted in grey without any stability information.

Although comparing Figures 12b,d shows some improvement is gained by taking higher order centered difference approximations, this improvement is not as pronounced as for the holistic models on this coarse grid as shown in Figures 12a,c. Both the 2nd order and 4th order centered difference approximations fail to reproduce the correct behaviour of the unstable trimodal and quadrimodal branches. In contrast, even the 5 point stencil  $\mathcal{O}(\gamma^3, \alpha^2)$  holistic approximation qualitatively reproduces the trimodal and quadrimodal branches on the same coarse grid. The values at which the bifurcation points occur are listed in Table 1 and confirm these holistic models outperform the centered difference approximations on this coarse grid of 8 elements on  $[0, \pi]$ .

### 4.2.3 Grid refinement improves accuracy

Since the equivalent PDE's, (24), (26) and (28), for our holistic models are of  $\mathcal{O}(h^2)$ ,  $\mathcal{O}(h^4)$  and  $\mathcal{O}(h^6)$  respectively, grid refinement should result in improved accuracy.

Figure 13 shows the bifurcation diagrams of the holistic models up to and including the  $\mathcal{O}(\gamma^4, \alpha^3)$  model on a finer grid of 12 elements on  $[0, \pi]$ . Compare Figure 13 with Figure 11 to confirm the improved accuracy for the holistic models on this refined grid. Table 1 also shows the bifurcation points are more accurately reproduced for the holistic models on this refined grid.

Figure 14 is a side by side comparison of the bifurcation diagrams of the  $\mathcal{O}(\gamma^4, \alpha^2)$  holistic model and the 4th order centered difference approximation (21). The accurate bifurcation diagram is shown in grey. See the

Figure 14: Bifurcation diagrams for (a)  $\mathcal{O}(\gamma^4, \alpha^2)$  holistic model, (b) 4th order centered difference approximations with 12 elements on the interval  $[0, \pi]$

$\mathcal{O}(\gamma^4, \alpha^2)$  holistic model is more accurate for  $0 \leq \alpha \leq 70$  but the improvement is not as pronounced as it is on the coarser grid of 8 elements. We suggest that this is because the major benefit to using the holistic models comes from application on coarser grids where the subgrid scale modelling is more significant.

### 4.3 Comparison to Galerkin approximations

Here we investigate the traditional Galerkin and non-linear Galerkin approximations [14] for the Kuramoto–Sivashinsky equation (1) with the periodic and odd conditions (30). We find the holistic models compare well with the Galerkin methods. While the Galerkin methods are of superior accuracy for solving the Kuramoto–Sivashinsky system (1) with periodic boundary conditions, because of their global nature they lack the flexibility of the local nature of the holistic models. Although not explored here, this local nature of the holistic models empowers its use with physical boundary conditions [27] other than periodic.

Galerkin methods seek solutions in the form which is dominantly the superposition of  $m$  periodic, global modes:

$$u(x, t) = \sum_{k=1}^m b_k(t) \sin(kx). \quad (31)$$

**The  $m$ -mode traditional Galerkin** approximation [14] is

$$\frac{db_k}{dt} \approx (-4k^4 + \alpha k^2) b_k - \alpha \beta_k^m, \quad 1 \leq k \leq m, \quad (32)$$

where

$$\beta_k^m(b_1, \dots, b_m) = \frac{1}{2} \sum_{j=1}^m j b_j [b_{k+j} + \text{sign}(k-j) b_{|k-j|}]. \quad (33)$$

**The  $m$ -mode first iterate nonlinear Galerkin** approximation [14] is based upon the adiabatic approximation (35) for higher wavenumber modes  $k = m+1 : 2m$ , namely

$$\frac{db_k}{dt} \approx (-4k^4 + \alpha k^2) b_k - \alpha \beta_k^{2m}(b_1, \dots, b_m, \phi_{m+1}, \dots, \phi_{2m}), \quad (34)$$

for  $1 \leq k \leq m$ , where

$$\phi_j = -\frac{\alpha}{4j^4} \beta_j^{2m}(b_1, \dots, b_m, 0, \dots, 0), \quad (35)$$

Figure 15: Bifurcation diagrams for (a) 3 mode, (b) 4 mode, (c) 6 mode and (d) 8 mode traditional Galerkin approximations on  $[0, \pi]$ .

Figure 16: Bifurcation diagrams for (a) 3 mode, (b) 4 mode, (c) 6 mode and (d) 8 mode first iterate nonlinear Galerkin approximations on  $[0, \pi]$ .

for  $m + 1 \leq j \leq 2m$  and  $\beta_j^{2m}$  is given by (33).

Obtain higher order nonlinear Galerkin approximations [22] through recognising time derivatives of these and even higher wave number modes. We do not explore these.

Now examine the bifurcation diagrams of the two Galerkin approximations (31–35) for  $0 \leq \alpha \leq 70$  and compare with the bifurcation diagrams of the holistic models on coarse grids, presented in §4.2. Figure 15 shows the Bifurcation diagrams for the 3 mode, 4 mode, 6 mode and 8 mode traditional Galerkin approximations on  $[0, \pi]$ . See that at least 4 modes are needed to qualitatively reproduce the behaviour of the stable bimodal branch. Compare the  $\mathcal{O}(\gamma^5, \alpha^2)$  holistic model with 6 elements from Figure 10a, to the 6 mode traditional Galerkin approximation and observe the  $\mathcal{O}(\gamma^5, \alpha^2)$  holistic model qualitatively models most steady state dynamics that are reproduced by the 6 mode traditional Galerkin approximation. Neither the  $\mathcal{O}(\gamma^5, \alpha^2)$  holistic model nor the 6 mode traditional Galerkin approximation qualitatively reproduce the correct behaviour of the unstable quadrimodal branch. Similarly the  $\mathcal{O}(\gamma^5, \alpha^2)$  holistic model with 8 elements from Figure 9a and the 8 mode traditional Galerkin approximation qualitatively model most steady state dynamics. However, the 8 mode traditional Galerkin approximation is more accurate.

Figure 16 shows the bifurcation diagrams for the 3 mode, 4 mode, 6 mode and 8 mode first iterate nonlinear Galerkin approximations (34) on  $[0, \pi]$ . See impressive accuracy for the low mode first iterate nonlinear Galerkin approximations. The 6 mode nonlinear Galerkin approximation reproduces all of the steady state dynamics for the range  $0 \leq \alpha \leq 70$ . There is no discernible difference between the bifurcation diagram of the 8 mode nonlinear Galerkin approximation and the accurate bifurcation diagram for this range of  $\alpha$ . Table 2 lists the values of nonlinearity parameter  $\alpha$  at which bifurcation points occur for the coarse grid holistic models and the Galerkin approximations [14]. The low mode first iterate nonlinear Galerkin approximations are impressively accurate.

This evidence suggests that the holistic models are competitive with traditional Galerkin approximations, but that nonlinear Galerkin models are

Table 2:  $\alpha$  values at which bifurcation points occur for the various coarse grid holistic models and low mode Galerkin approximations

Approximation	$R_2b_1$	$R_2b_2$	$R_2b_3$	$R_2b_4$	$R_3t_1$	$R_3t_2$	$R_4b_1$	$R_4q_1$
Accurate 48pts								
6th order	16.14	22.56	52.89	63.74	36.23	50.91	64.56	64.28
Holistic 8 elements								
$\mathcal{O}(\gamma^3, \alpha^2)$	14.64	20.36	39.34	44.96	29.28*	—	45.28	44.87
$\mathcal{O}(\gamma^3, \alpha^3)$	14.65	20.52	39.66	45.16	29.33*	—	45.47	44.96
$\mathcal{O}(\gamma^3, \alpha^4)$	14.65	20.53	39.72	45.21	29.33*	—	45.51	44.97
$\mathcal{O}(\gamma^4, \alpha^2)$	16.00	22.56	48.62	57.38	34.73*	—	57.89	57.49
$\mathcal{O}(\gamma^4, \alpha^3)$	16.00	22.56	48.25	56.84	34.73*	—	57.45	57.28
$\mathcal{O}(\gamma^4, \alpha^4)$	16.00	22.57	48.10	56.63	34.73*	—	57.30	57.21
$\mathcal{O}(\gamma^5, \alpha^2)$	16.13	22.72	51.54	61.54	35.89*	—	62.20	61.78
$\mathcal{O}(\gamma^5, \alpha^3)$	16.13	22.73	51.53	61.37	35.91*	—	62.04	61.70
$\mathcal{O}(\gamma^5, \alpha^4)$	16.13	22.73	51.60	61.38	35.91*	—	62.02	61.69
Holistic 12 elements								
$\mathcal{O}(\gamma^3, \alpha^2)$	15.45	21.67	45.96	53.94	32.86	45.98	54.49	54.17
$\mathcal{O}(\gamma^3, \alpha^3)$	15.45	21.69	46.05	54.00	32.87	46.33	54.55	54.20
$\mathcal{O}(\gamma^4, \alpha^2)$	16.11	22.62	51.93	62.10	35.90	50.92	62.83	62.52
$\mathcal{O}(\gamma^4, \alpha^3)$	16.11	22.62	51.94	62.10	35.90	50.94	62.83	62.52
Galerkin [14]								
3-m Euler–Galerkin	16.10	20.59	246.14	—	36.21	—	—	—
3-m Pseudo-stdy II	16.13	21.93	102.90	—	36.21	—	—	—
3-m Pseudo-stdy	16.13	22.01	93.91	—	36.24	63.91	—	—
12-m traditional	16.14	22.56	52.89	63.74	36.23	50.91	64.56	64.28
6-m traditional	16.14	22.55	52.72	63.28	36.23	46.85	64.00	64.00
3-m traditional	16.14	16.00	16.0??	16.0	36.00	36.0	—	—

significantly better. However, recall that the holistic models are based upon analysis of local dynamics and thus we expect them to be more flexibly useful in applications than the global methods of these Galerkin approximations.

#### 4.4 Coarse grids allow large time steps

A major benefit of accurate models on coarse grids is that larger time steps are possible while maintaining numerical stability. §4.2 shows the remarkable accuracy of the  $\mathcal{O}(\gamma^5, \alpha^2)$  holistic model (19) on a coarse grid of 8 elements. Here we investigate the maximum stable time step for *explicit* Runge–Kutta time integration on various holistic models—implicit integration schemes are not considered.

In particular we compare approximations of similar accuracy but different grid resolutions to demonstrate the superior performance of the holistic

Figure 17: Bifurcation diagrams of (a)  $\mathcal{O}(\gamma^5, \alpha^2)$  holistic model, with 8 elements on  $[0, \pi]$ , and (b) 2nd order centered difference approximation with 16 grid points on  $[0, \pi]$ . Accurate bifurcation diagram is shown in grey.

Table 3: Approximate maximum time steps for stability of 4th order Runge–Kutta scheme.

Approximation	$\alpha = 10$	$\alpha = 20$	$\alpha = 30$
Holistic 8 elements			
$\mathcal{O}(\gamma^3, \alpha^2)$	.0011	.0014	.0017
$\mathcal{O}(\gamma^3, \alpha^3)$	.0011	.0014	.0017
$\mathcal{O}(\gamma^3, \alpha^4)$	.0011	.0014	.0017
$\mathcal{O}(\gamma^4, \alpha^2)$	.0006	.0007	.0008
$\mathcal{O}(\gamma^4, \alpha^3)$	.0006	.0007	.0008
$\mathcal{O}(\gamma^4, \alpha^4)$	.0006	.0007	.0008
$\mathcal{O}(\gamma^5, \alpha^2)$	.0005	.0005	.0006
$\mathcal{O}(\gamma^5, \alpha^3)$	.0005	.0005	.0006
$\mathcal{O}(\gamma^5, \alpha^4)$	.0005	.0005	.0006
Centered 8 points			
2nd order	.0011	.0012	—
4th order	.0006	.0007	.0008
6th order	.0005	.0005	.0006
Centered 16 points			
2nd order	.00006	.00006	.00006

models. For example, Figure 17 compares the bifurcations diagrams of the  $\mathcal{O}(\gamma^5, \alpha^2)$  holistic model with 8 elements on  $[0, \pi]$  and the 2nd order centered difference approximation (20) with 16 grid points on  $[0, \pi]$ . The accurate bifurcation diagram is shown in grey. See that the  $\mathcal{O}(\gamma^5, \alpha^2)$  holistic model on the coarse grid is of similar accuracy to the 2nd order centered difference approximation on the more refined grid. Thus a reasonable comparison of computability is made using these two schemes.

Numerical experiments used the 4th order Runge–Kutta scheme to estimate the maximum stable time step for different holistic models and centered difference approximations at various values of nonlinearity parameter  $\alpha$ . Table 3 lists the approximate maximum time steps that maintain numerical stability along both the negative unimodal branch at  $\alpha = 10$ , and the negative bimodal branch at  $\alpha = 20$  and  $\alpha = 30$ . For the  $\mathcal{O}(\gamma^5, \alpha^2)$  holistic model with 8 elements, the maximum time step maintaining numerical sta-

bility is approximately 10 times larger than the corresponding time step for the 2nd order centered difference approximation with 16 grid points. The  $\mathcal{O}(\gamma^5, \alpha^2)$  holistic model requires approximately 3 times the number of floating point operations per grid value at each time step compared to the 2nd order centered difference approximation. However, on a coarse grid of 16 points the 2nd order centered difference approximation must be applied at twice as many grid points. Thus the  $\mathcal{O}(\gamma^5, \alpha^2)$  holistic model can be integrated an order of magnitude faster than the 2nd order centered difference approximation while maintaining similar accuracy.

Note: Table 3 shows that the higher order terms in the nonlinearity  $\alpha$ , generated by the holistic method, do not reduce numerical stability. Wider stencil holistic approximations reduce the maximum stable time step somewhat, but so do the wider stencil conventional centered difference approximations. Thus, bear in mind that we need to balance the accuracy gained by using higher order approximation in  $\gamma$ , that is, wider stencil approximations, with the reduction in numerical stability and the increase in computation per grid value.

## 5 Holistic models are accurate for time dependent phenomena

The Kuramoto–Sivashinsky equation (1) has rich dynamics [16, 14, 15, 30, 5, 12, 6, 2]. Having established the excellent performance of the holistic models in reproducing the steady states of the Kuramoto–Sivashinsky system in Section 4, we now investigate the holistic models performance at reproducing time dependent phenomena. The Kuramoto–Sivashinsky system exhibits complex time dependent behaviour such as limit cycles, period doubling and spatio-temporal chaos. This provides us with an example to explore the holistic approach to modelling time dependent phenomena with relatively coarse discretisations.

We restrict attention to  $2\pi$  periodic solutions,

$$u(x, t) = u(x + 2\pi, t). \quad (36)$$

Initially we restrict further to solutions with odd symmetry, as in the previous section, which exhibit, see Figure 6, Hopf bifurcations to limit cycle solutions, and subsequent period doubling bifurcations apparently leading to low-dimensional chaos [14, 15, 30]. In §5.1 we examine the dynamics of the holistic models on coarse grids through the eigenvalues of the models near



Figure 18: The four largest (least negative) eigenvalues along the stable bimodal branch for the (a)  $\mathcal{O}(\gamma^3, \alpha^2)$ , (b)  $\mathcal{O}(\gamma^4, \alpha^2)$ , (c)  $\mathcal{O}(\gamma^5, \alpha^2)$  holistic models shown in green for 8 elements on  $[0, \pi]$ . The accurate eigenvalues are shown in blue.

the steady states. For example, we see that the  $\mathcal{O}(\gamma^5, \alpha^2)$  holistic model reproduces much of the eigenvalue information for  $0 \leq \alpha \leq 70$  on a coarse grid of 8 elements. In §5.2 we explore the bifurcation diagrams near the first Hopf bifurcation and capture the stable limit cycles and period doubling sequence. The holistic models more accurately model the dynamics than centered difference approximations of equal stencil width. Subsequently we just require spatial periodicity whence stable travelling wave appear followed by, at higher values of nonlinearity parameter  $\alpha$ , more complex spatio-temporal chaos as investigated by Holmes, Lumley & Berkooz [12] and Dankowicz et al. [6]. In §5.3 we find the holistic discretisations more accurately model the amplitude and wave speed of travelling wave solutions, and predict better space time plots and time averaged power spectra, than corresponding the centered difference approximations.

## 5.1 Dynamics near the steady states are reproduced

Consider the eigenvalues of the Kuramoto–Sivashinsky system (1) linearised about the the steady states and restricted to odd symmetry. Accurate modelling of the eigenvalues near the steady states is a necessary condition for the accurate modelling of the dynamics. We look at two views of the eigenvalues: first, their value on the negative bimodal branch; and second a more qualitative plot of their values on the entire bifurcation diagram for nonlinearity parameter  $0 \leq \alpha \leq 70$ .

**Compare eigenvalues along the bimodal branch** We investigate dynamics near the stable negative bimodal branch. Consider the real part of the four largest (least negative real part) eigenvalues for low order holistic models and compare to explicit centered difference approximations on a coarse grid of 8 elements on  $[0, \pi]$ . Figure 18 shows the four largest eigenvalues for the  $\mathcal{O}(\gamma^3, \alpha^2)$  (15),  $\mathcal{O}(\gamma^4, \alpha^2)$  (18) and  $\mathcal{O}(\gamma^5, \alpha^2)$  (19) holistic models in green and the accurate solution in blue.<sup>5</sup> Recall the  $\mathcal{O}(\gamma^3, \alpha^2)$ ,  $\mathcal{O}(\gamma^4, \alpha^2)$

<sup>5</sup>As in Section 4, the accurate reference for solutions is found using a 6th order centered difference approximation with 48 grid points on  $[0, \pi]$ .



Figure 19: The four largest eigenvalues along the stable bimodal branch for the (a) 2nd order, (b) 4th order, (c) 6th order centered difference approximations shown in magenta for 8 grid points on  $[0, \pi]$ . The accurate eigenvalues are shown in blue.

Figure 20: Bifurcation diagram of the  $\mathcal{O}(\gamma^5, \alpha^2)$  holistic model with 8 elements and odd symmetry on  $[0, \pi]$ , depicting the real parts of the 8 largest (least negative) eigenvalues colour coded according to the colour bar shown.

and  $\mathcal{O}(\gamma^5, \alpha^2)$  holistic models have 5 point, 7 point and 9 point stencils, respectively. Figure 18c, shows the four largest eigenvalues for the  $\mathcal{O}(\gamma^5, \alpha^2)$  holistic model closely matches the accurate solution over this range of non-linearity parameter  $\alpha$ .

Similarly, Figure 19 shows the four largest eigenvalues for the 2nd order (20), 4th order (21) and 6th order (22) centered difference approximations in magenta on the same coarse grid. The centered difference approximations shown here are of equal stencil width to the corresponding holistic models in Figure 18. Figure 19a, shows the 2nd order centered difference barely approximates the behaviour of the stable bimodal branch for  $\alpha < 20$ . Even the 6th order centered difference approximation, Figure 19c, is inferior to the  $\mathcal{O}(\gamma^4, \alpha^2)$  holistic model for  $\alpha > 30$ . This is despite the 6th order centered difference model having a wider stencil of 9 points compared to the 7 point stencil of the  $\mathcal{O}(\gamma^4, \alpha^2)$  holistic model. Figures 18 and 19 show the low order holistic models are superior to the corresponding centered difference approximations for reproducing the dynamics near the stable bimodal branch.

**Compare eigenvalues across the bifurcation diagram** Here we explore a new view of the earlier bifurcation diagrams that additionally depicts the *real part* of the 8 largest (least negative) eigenvalues by colour. Compare the eigenvalues of the  $\mathcal{O}(\gamma^5, \alpha^2)$  (19) holistic model, see Figure 20, on the coarse grid of 8 elements on  $[0, \pi]$  to accurate ones for the Kuramoto–Sivashinsky system, see Figure 21, over the nonlinearity parameter  $0 \leq \alpha \leq 70$ . The magnitude of the real part of the eigenvalues is colour coded according to the

Figure 21: Bifurcation diagram of the accurate Kuramoto–Sivashinsky system, depicting the real parts of the 8 largest (least negative) eigenvalues, colour coded according to the colour bar shown.

Figure 22: Bifurcation diagrams near the first Hopf bifurcation for (a)  $\mathcal{O}(\gamma^3, \alpha^2)$ , (b)  $\mathcal{O}(\gamma^4, \alpha^2)$ , (c)  $\mathcal{O}(\gamma^5, \alpha^2)$  holistic models with 8 elements on  $[0, \pi]$  and (d) an accurate bifurcation diagram. Stable limit cycles are shown in light blue and unstable limit cycles are shown in orange.

colour bar shown on the right of the bifurcation diagram; the least negative eigenvalues are plotted above the more negative to give a small band of colour for each branch of steady states at each parameter value. Similarly to the bifurcation diagrams shown in Section 4, the open squares denote bifurcation points and the black squares denote Hopf bifurcations. Figure 20, when compared to Figure 21, shows that in addition to reproducing the stability of the accurate Kuramoto–Sivashinsky system for  $0 \leq \alpha \leq 70$  as discussed in §4.2, the  $\mathcal{O}(\gamma^5, \alpha^2)$  holistic model reproduces well the eigenvalues for most of this range of nonlinearity parameter  $\alpha$ . This accurate modelling of the eigenvalues is evidence of accurate modelling of the Kuramoto–Sivashinsky dynamics, at least near the steady states.

## 5.2 Extend the Hopf bifurcations

Hopf bifurcations give rise to time periodic solutions (limit cycles). We explore the predictions of the various models to see how well they capture these strongly time dependent phenomena.

Here we investigate the bifurcation diagrams obtained by extending the first Hopf bifurcation, at  $\alpha = 30.345$ , on the positive bimodal branch and the period doubling sequence that ensues. We compare the bifurcation diagrams of low order holistic models to explicit centered difference models on a coarse grid of 8 elements on  $[0, \pi]$  to the accurate bifurcation diagram of the Kuramoto–Sivashinsky system. Trajectories in the period doubling sequence are reported and compared by MacKenzie [19]. As before, the holistic models outperform the corresponding centered difference approximations.

**Investigate the first Hopf bifurcation** We now investigate the holistic models near the first Hopf bifurcation on the positive bimodal branch, labeled  $\text{HB}_1$ , with a coarse grid of 8 elements on  $[0, \pi]$ . Figure 22 shows the bifurcation diagrams of the low order holistic models and the accurate bifurcation diagram near the first Hopf bifurcation. The stable limit cycles (light blue) that continue from this bifurcation point undertake a period doubling sequence commencing at a point labeled PD (yellow square). The pair of

Figure 23: Bifurcation diagrams near the first Hopf bifurcation for (a) 4th order, (b) 6th order centered difference approximations with 8 grid points on  $[0, \pi]$ . Stable limit cycles are shown in light blue and unstable limit cycles are shown in orange.

unstable limit cycles born at PD give rise to the period doubling sequence leading to chaos.

The accurate bifurcation diagram shown in Figure 22d, is produced using a 6th order centered difference approximation with 24 grid points on  $[0, \pi]$ . The accurate bifurcation diagram shown is identical to the bifurcation diagram for the same range of  $\alpha$  produced by Jolly et al. [14]. Figure 22a, shows that even the lowest order  $\mathcal{O}(\gamma^3, \alpha^2)$  (15) holistic model reproduces the the first Hopf bifurcation and finds the period doubling point on this coarse grid of 8 elements<sup>6</sup> In comparison, the corresponding 2nd order centered difference approximation does not even have the first Hopf bifurcation, see Figure 12b.

Figure 22b,c, show that higher order holistic models accurately model the first Hopf bifurcation and the resulting stable and unstable limit cycles. The accuracy of the  $\mathcal{O}(\gamma^5, \alpha^2)$  (19) holistic model for reproducing these periodic solutions of the Kuramoto–Sivashinsky system is remarkable on this coarse grid. Figure 23 shows the corresponding bifurcation diagrams for the 4th order and 6th order centered difference approximations with 8 grid points on  $[0, \pi]$ . Compare Figure 23 and Figure 22 to see that the 6th order centered difference approximation which has a nine point stencil does not perform as well as the  $\mathcal{O}(\gamma^4, \alpha^2)$  (18) holistic model which has a 7 point stencil. Figure 22b,c, show that higher order holistic models more accurately model the first Hopf bifurcation and the resulting stable and unstable limit cycles. The accuracy of the  $\mathcal{O}(\gamma^5, \alpha^2)$  (19) holistic model for reproducing these periodic solutions of the Kuramoto–Sivashinsky system is remarkable on this coarse grid. Table 4 shows the parameter values  $\alpha$  for the Hopf bifurcations, HB<sub>1</sub> and the initial period doubling point PD. See that both the  $\mathcal{O}(\gamma^4, \alpha^2)$  and  $\mathcal{O}(\gamma^5, \alpha^2)$  holistic models are more accurate than the 4th order and 6th order centered difference approximations in reproducing the first Hopf bifurcation and the resulting period doubling point.

---

<sup>6</sup>Figure 22a displays the bifurcation diagram for  $25 \leq \alpha \leq 32$  compared to  $30 \leq \alpha \leq 37$  for the other diagrams. Since the first Hopf bifurcation for the  $\mathcal{O}(\gamma^3, \alpha^2)$  holistic model occurs at  $\alpha = 25.595$  the bifurcation diagram is shifted to contain the important dynamics.

Table 4: Nonlinearity parameter  $\alpha$  values for the first Hopf bifurcation point HB<sub>1</sub> and resulting period doubling point PD.

Approximation	HB <sub>1</sub>	PD
Holistic 8 elements		
$\mathcal{O}(\gamma^3, \alpha^2)$	25.60	27.22
$\mathcal{O}(\gamma^4, \alpha^2)$	30.04	32.03
$\mathcal{O}(\gamma^5, \alpha^2)$	30.66	32.95
Centered 8 points		
2nd order	—	—
4th order	27.91	29.57
6th order	29.11	31.40
Accurate	30.35	32.97

Figure 24:  $\alpha = 5$ : wave-like solutions at  $t = 0, 0.2, 0.4, 0.6, 0.8, 1$  for the  $\mathcal{O}(\gamma^3, \alpha^2)$  holistic model shown in green and the 2nd order centered difference approximation in magenta on a coarse grids of 8 elements on  $[0, 2\pi]$ . The accurate solution is shown in blue.

### 5.3 Dynamics of periodic patterns without odd symmetry

Consider the Kuramoto–Sivashinsky system (1) with solutions that are spatially periodic (36). We remove the requirement for odd symmetry. Consequently, we now explore travelling wave like solutions at low nonlinearity  $\alpha$ . Also, we investigate the spatio-temporal chaos that occurs at higher  $\alpha$ .

**Good performance for holistic models at low  $\alpha$**  Consider the holistic models of the Kuramoto–Sivashinsky system (1) and (36) for nonlinearity parameter  $\alpha = 5$  and  $\alpha = 10$  on coarse grids of 8 elements on  $[0, 2\pi]$ . Figure 24 shows solutions obtained from the lowest order  $\mathcal{O}(\gamma^3, \alpha^2)$  (15) holistic model for  $\alpha = 5$  in green, the accurate solution in blue and the corresponding 2nd order centered difference approximation (20) with 8 points on  $[0, 2\pi]$ , in magenta. The solutions are shown at time slices  $t = 0, 0.2, 0.4, 0.6, 0.8, 1$ , starting from the half-wave initial condition of  $u(x, 0) = |\sin(x/2)|$ . See the  $\mathcal{O}(\gamma^3, \alpha^2)$  holistic model is superior to the 2nd order centered difference approximation on this coarse grid. In particular, the amplitude of the evolving wave-like solution and the wave speed are more accurately reproduced by the  $\mathcal{O}(\gamma^3, \alpha^2)$  holistic model for  $\alpha = 5$ .

Figure 25:  $\alpha = 10$ : wave-like solutions at  $t = 0, 0.2, 0.4, 0.6, 0.8, 1$  for the  $\mathcal{O}(\gamma^3, \alpha^2)$ ,  $\mathcal{O}(\gamma^4, \alpha^2)$  and  $\mathcal{O}(\gamma^5, \alpha^2)$  holistic models shown in green, light green and light blue respectively and the 6th order centered difference approximation shown in red on a coarse grids of 8 elements on  $[0, 2\pi]$ . The accurate solution is shown in blue.

Similarly, Figure 25 shows the same time slices for larger  $\alpha = 10$ . The  $\mathcal{O}(\gamma^3, \alpha^2)$  (15) holistic model is shown in green, the  $\mathcal{O}(\gamma^4, \alpha^2)$  (18) model is shown in light green and the  $\mathcal{O}(\gamma^5, \alpha^2)$  (19) holistic model in light blue for this coarse grid of 8 elements on  $[0, 2\pi]$ . For this  $\alpha$  the 2nd order (20) and 4th order (21) centered difference approximations do not generate a wave-like solution at all. However, the 6th order centered difference approximation (22) does produce the travelling wave-like solution shown in red. The  $\mathcal{O}(\gamma^3, \alpha^2)$  holistic model (green) is the least accurate on this coarse grid but it does reproduce a stable solution on this coarse grid for only a 5 point stencil approximation. The  $\mathcal{O}(\gamma^4, \alpha^2)$  holistic model (light green) more accurately models the amplitude of the solution compared to the 6th order centered difference approximation despite having a smaller stencil width. The  $\mathcal{O}(\gamma^5, \alpha^2)$  holistic model is the most accurate at reproducing both the amplitude and the wave speed of the stable wave-like solution for  $\alpha = 10$  on this coarse grid of 8 elements.

**Good performance for more complex behaviour** For higher values of nonlinearity parameter  $\alpha$  for which the Kuramoto–Sivashinsky system exhibits more complex behaviour, including spatio-temporal chaos, it is more useful to compare time averaged power spectra rather than particular travelling waves. Here we investigate the performance of the holistic models on coarse grids for  $\alpha = 20$  and  $50$  using the example of the  $\mathcal{O}(\gamma^5, \alpha^2)$  (19) holistic model on relatively coarse grids, and we compare it with the 6th order centered difference approximation which is of equal stencil width. The focus here is to show the improved performance of the holistic models for ranges of parameter  $\alpha$  that contain more complex time dependent behaviour. We also expect a corresponding improvement for the other holistic models but this is not investigated here. Further, we also compare the  $\mathcal{O}(\gamma^5, \alpha^2)$  holistic model on coarse grids to the 2nd order centered difference approximations of similar accuracy. We find the  $\mathcal{O}(\gamma^5, \alpha^2)$  holistic model, but with approximately 1/3 of the grid points, has comparable accuracy to 2nd order centered difference approximations.

Figure 26 shows space time plots of (a) the  $\mathcal{O}(\gamma^5, \alpha^2)$  holistic model

Figure 26:  $\alpha = 20$ : space time plots for (a) the  $\mathcal{O}(\gamma^5, \alpha^2)$  holistic model with 12 elements on  $[0, 2\pi]$ , (b) 6th order centered difference approximation with 12 grid points on  $[0, 2\pi]$  and (c) the accurate solution

Figure 27:  $\alpha = 20$ : time averaged power spectra for the  $\mathcal{O}(\gamma^5, \alpha^2)$  holistic model with 12 elements on  $[0, 2\pi]$  shown in light blue, and the 6th order centered difference approximation in red for (a) 12 grid points on  $[0, 2\pi]$  and (b) 16 grid points on  $[0, 2\pi]$ . The accurate power spectrum is shown in blue.

with 12 elements on  $[0, 2\pi]$ , (b) the 6th order centered difference approximation with 12 grid points on  $[0, 2\pi]$  and (c) the accurate solution.<sup>7</sup> See the  $\mathcal{O}(\gamma^5, \alpha^2)$  holistic model reproduces much of the complex structure of the accurate solution for  $\alpha = 20$  with 12 elements. Figure 26b, shows the 6th order centered difference approximation incorrectly finds a periodic solution after approximately  $t = 0.2$ .

Since the Kuramoto–Sivashinsky system at nonlinearity parameter  $\alpha = 20$  exhibits more complex time dependent behaviour than simple limit cycles, we compare time averaged power spectra, denoted here by  $S(k)$  for wavenumber  $k$ . Figure 27a, shows a log-log plot of the time average power spectra of the  $\mathcal{O}(\gamma^5, \alpha^2)$  holistic model in light blue and the 6th order centered difference approximation on a coarse grid of 12 elements on  $[0, 2\pi]$  in red. The accurate power spectrum is shown in blue. For this coarse grid of only 12 elements only 5 wavenumbers are relevant, as displayed. See that the  $\mathcal{O}(\gamma^5, \alpha^2)$  holistic model is superior to the 6th order centered difference approximation on this coarse grid of 12 elements. Figure 27b, compares the time average power spectrum of the  $\mathcal{O}(\gamma^5, \alpha^2)$  holistic model in light blue with 12 elements and the 6th order centered difference approximation with 16 grid points. The  $\mathcal{O}(\gamma^5, \alpha^2)$  holistic model achieves similar accuracy on a coarser grid.

---

<sup>7</sup>The accurate solutions plotted in this section are computed using a 6th order centered difference approximation and 256 grid points on the interval  $[0, 2\pi]$ . This is sufficient grid resolution to capture the important dynamics of the Kuramoto–Sivashinsky system for the values of  $\alpha$  investigated here.

Figure 28:  $\alpha = 20$ : time averaged power spectra for for the  $\mathcal{O}(\gamma^5, \alpha^2)$  holistic model with 12 elements on  $[0, 2\pi]$  shown in light blue, and the 2nd order centered difference approximation in magenta for (a) 24 grid points on  $[0, 2\pi]$  and (b) 36 grid points on  $[0, 2\pi]$ . The accurate spectrum is shown in blue.

Figure 29:  $\alpha = 50$ : space time plots for (a) the  $\mathcal{O}(\gamma^5, \alpha^2)$  holistic model with 24 elements on  $[0, 2\pi]$ , (b) 6th order centered difference approximation with 24 grid points on  $[0, 2\pi]$  and (c) the accurate solution.

Figure 30:  $\alpha = 50$ : time averaged power spectra for the  $\mathcal{O}(\gamma^5, \alpha^2)$  holistic model with 24 elements on  $[0, 2\pi]$  shown in light blue, and the 6th order centered difference approximation in red for (a) 24 grid points on  $[0, 2\pi]$  and (b) 32 grid points on  $[0, 2\pi]$ . The accurate spectrum is shown in blue.

The power spectra of the  $\mathcal{O}(\gamma^5, \alpha^2)$  holistic model on a coarse grid of 12 elements and the 2nd order centered difference approximation on the more refined grids of 24 and 36 points are shown in Figures 27a,b respectively. See a refined grid of 36 points is needed achieve similar accuracy to the  $\mathcal{O}(\gamma^5, \alpha^2)$  holistic model on a coarse grid of 12 elements on  $[0, 2\pi]$ . That is, through its subgrid scale modeling, the holistic model achieves similar accuracy with one-third the dimensionality.

For nonlinearity parameter  $\alpha = 50$  the Kuramoto–Sivashinsky system exhibits even more complex behaviour, see the space time plots in Figure 29. The  $\mathcal{O}(\gamma^5, \alpha^2)$  holistic model more accurately reproduces the Kuramoto–Sivashinsky system than the 6th order centered difference approximation on this coarse grid of 24 elements. On this coarse grid the 6th order centered difference approximation shown in Figure 29b, exhibits a periodic solution after time  $t \approx 0.1$  which does not match the irregular behaviour seen in the accurate solution and the  $\mathcal{O}(\gamma^5, \alpha^2)$  holistic model.

We again examine time averaged power spectra to further investigate the performance of the  $\mathcal{O}(\gamma^5, \alpha^2)$  holistic model at this relatively large parameter value of  $\alpha = 50$ . Figure 30 compares the time averaged power spectrum of the  $\mathcal{O}(\gamma^5, \alpha^2)$  holistic model in light blue on a coarse grid of 24 elements on  $[0, 2\pi]$  to the 6th order centered difference approximation in red, for (a) 24 grid points and (b) 32 grid points on  $[0, 2\pi]$ . The 6th order centered difference approximation with 32 grid points has similar accuracy to the  $\mathcal{O}(\gamma^5, \alpha^2)$  holistic model on a coarse grid of just 24 elements for  $\alpha = 50$ .

This investigation of the  $\mathcal{O}(\gamma^5, \alpha^2)$  holistic model on coarse grids for  $\alpha = 20$  and 50 shows it reproduces similar accuracy to the 2nd order centered difference approximation on a coarse grid of approximately 1/3 the resolution, and similar accuracy to the 6th order centered difference approximation on grids of approximately 3/4 the resolution. MacKenzie [19] reports that even at  $\alpha = 200$  the holistic model qualitatively well captures the dynamics of the



Kuramoto–Sivashinsky PDE. This increased accuracy on coarse grids allows larger time steps for explicit time integration schemes, as discussed in §4.4.

## 6 Conclusion

Holistic discretisation [25] is straightforwardly extended to fourth order dissipative PDEs through the example of the Kuramoto–Sivashinsky equation [18]. We divide the domain into elements by introducing artificial internal boundary conditions (§2) which isolate the elements when  $\gamma = 0$  but when  $\gamma = 1$  they fully couple the elements to recover the Kuramoto–Sivashinsky equation. Then centre manifold theory supports the discretisation, see §2.2. The holistic models listed in §3 have a dual justification (§3.3): not only are they supported by centre manifold theory for finite element size  $h$ , the IBCs are specially crafted [26] so the models are also consistent with the Kuramoto–Sivashinsky equation as the grid spacing  $h \rightarrow 0$ .

No formal error bounds currently exist for the holistic method; the difficulty is that the models are based at  $\gamma = 0$  but are evaluated at finite  $\gamma = 1$ . Instead we present a detailed numerical investigation of the holistic models of the steady states (Section 4) and time dependent solutions (Section 5) of the Kuramoto–Sivashinsky on coarse grids.

We compared, in §4.4, the accuracy of different approximations in predicting steady states on different grid resolutions. The holistic  $\mathcal{O}(\gamma^5, \alpha^2)$  approximation on a grid of 8 elements has similar accuracy to a 2nd order centered difference approximation on a grid of 16 points. Consequently the holistic model allows a maximum time step which is an order of magnitude longer than that of the explicit centered difference approximation of similar accuracy, while maintaining numerical stability. The accuracy of the holistic approximations to the Kuramoto–Sivashinsky equation on coarse grids and subsequent improved performance justifies further application of the holistic method and future investigation of the approach.

The holistic models on coarse grids also modelled well time dependent phenomena of the Kuramoto–Sivashinsky system. In particular, in §5.1 we saw the holistic models more accurately model the eigenvalues near the steady states of the first form of the Kuramoto–Sivashinsky system compared to explicit centered difference approximations of equal stencil widths. The coarse grid holistic models also more accurately model the first Hopf bifurcation and the resulting period doubling sequence, see §5.2. Further, in comparison with explicit centered difference models, in §5.3, we saw good performance for higher values of the nonlinearity parameter  $\alpha$  and more accurate predictions



of time averaged power spectra: the  $\mathcal{O}(\gamma^5, \alpha^2)$  holistic model achieves similar accuracy to the 2nd order and 6th order centered difference approximations on approximately 1/3 and 3/4 of the grid resolutions respectively.

This good performance of the holistic models for accurately reproducing both the steady states and the time dependent phenomena of the Kuramoto–Sivashinsky system is good evidence that the holistic approach is a powerful method for discretising dissipative PDEs on coarse grids.

## A Computer algebra derives the discretisation

```

1 write "The holsitic discretisation of a supplied PDE. "$
2 write "based on holistic PDE version beta.1, 20 Dec 2001"$
3
4 stenwidth:=9;
5 epsilon:=2;
6
7 % improve printing
8 linelength 72$
9 on div; off allfac; on revpri;
10 factor gamma,h;
11
12 % make function of xi=(x-x_j)/h
13 depend xi,x;
14 let df(xi,x)=>1/h;
15
16 % get parameters of the PDE
17 write "The parameters of the PDE follow"$
18 operator uu;
19 depend uu,x;
20 dissipate:=df(uu,x,4);
21 discof:=-4;
22 % set neglected orders of errors
23 if stenwidth=3 then let gamma^2=>0
24 else if stenwidth=5 then let gamma^3=>0
25 else if stenwidth=7 then let gamma^4=>0
26 else if stenwidth=9 then let gamma^5=>0
27 else if stenwidth=11 then let gamma^6=>0
28 else if stenwidth=13 then let gamma^7=>0
29 else if stenwidth=15 then let gamma^8=>0
30 else if stenwidth=17 then let gamma^9=>0

```

```

31 else if stenwidth=27 then let gamma^15=>0
32 else let gamma=>0$
33 if epsilo=decreasing then epsilon:=gamma
34 else if epsilo=2 then let a^2=>0
35 else if epsilo=3 then let a^3=>0
36 else if epsilo=4 then let a^4=>0
37 else if epsilo=5 then let a^5=>0
38 else let a=>0$
39
40 %decreasing:=1$
41 operator u;
42
43 % solvability condition
44 operator solg; linear solg;
45 let { solg(xi^~p,xi)=>(1+(-1)^p)/(p+2)/(p+1)
46       , solg(xi,xi)=>0, solg(1,xi)=>1 };
47
48 % define solving operator depending upon the dissipation
49 operator solv; linear solv;
50 if sub(uu=x^9,dissipate)=72*x^7 then begin
51 write disorder:=2;
52 % solves v''=RHS s.t. v(0)=0 and v(+1)=v(-1)
53 let { solv(xi^~p,xi) =>
54       ( xi^(p+2)-(1-(-1)^p)*xi/2 )/(p+1)/(p+2)
55       , solv(xi,xi) => (xi^3-xi)/6
56       , solv(1,xi) => (xi^2)/2 };
57 end else
58 if sub(uu=x^9,dissipate)=3024*x^5 then begin
59 write disorder:=4;
60 % solves v''''=RHS s.t. v(0)=v(+1)=v(-1)=0 and v(+2)=v(-2)
61 let { solv(xi^~p,xi) =>
62       ( xi^(p+4)-(1+(-1)^p)/2*xi^2
63         -(1-(-1)^p)/6*((2^(p+3)-1)*xi^3+(4-2^(p+3))*xi)
64         )/(p+1)/(p+2)/(p+3)/(p+4)
65       , solv(xi,xi) => (xi^5-(15*xi^3-12*xi)/3)/120
66       , solv(1,xi) => (xi^4-xi^2)/24 };
67 end else
68 if sub(uu=x^9,dissipate)=60480*x^3 then begin
69 write disorder:=6;
70 % solves v''''''=RHS s.t. v(0)=v(+1)=v(-1)=v(+2)=v(-2)=0 and v(+3)=v(-3)
71 let { solv(xi^~p,xi) =>
72       ( xi^(p+6)+(1+(-1)^p)/6*((2^(p+4)-4)*xi^2+(1-2^(p+4))*xi^4)
73         +(1-(-1)^p)/240*(4*(-45+9*2^(p+6))-3^(p+6))*xi

```

```

74             +5*(13-8*2^(p+6)+3^(p+6))*xi^3
75             +(-5+4*2^(p+6)-3^(p+6))*xi^5)
76             )/(p+1)/(p+2)/(p+3)/(p+4)/(p+5)/(p+6)
77     , solv(xi,xi) => (xi^7-36*xi+49*xi^3-14*xi^5)/5040
78     , solv(1,xi) => (xi^6+4*xi^2-5*xi^4)/720 };
79 end;
80 if disorder>stenwidth then
81 write "*** Warning: the stencil width is too small ***";
82
83
84 % parametrise with evolving uu(j)
85 depend u,t;
86 let df(u(~k),t)=>sub(j=k,gj);
87
88 % linear solution in jth element
89 write "Start with the linear approximation"$
90 uu:=u(j)+udash;
91 udash:=0;
92 gj:=0;
93 % iterative refinement to specified error
94 write "Iterate to make residuals negligible"$
95 iteration:=0$
96 let {u(j+4)=>-u(j+3),u(j+5)=>-u(j+2),u(j+6)=>-u(j+1)
97 ,u(j+7)=>-u(j),u(j-1)=>-u(j),u(j-2)=>-u(j+1)
98 ,u(j-3)=>-u(j+2),u(j-4)=>-u(j+3)};
99
100 repeat begin
101     write iteration:=iteration+1;
102     deq:=-df(uu,t)+discof*dissipate;%-a*(df(uu,x,2));
103     %uu*df(uu,x)+
104     rbc:=- (sub(xi=+1,uu)-sub(xi=0,uu))+gamma*(u(j+1)-u(j));
105     lbc:=- (sub(xi=0,uu)-sub(xi=-1,uu))+gamma*(u(j)-u(j-1));
106     ok:= if (deq=0)and(rbc=0)and(lbc=0) then 1 else 0;
107     if disorder>3 then begin
108     rrbc:=- (sub(xi=+2,uu)-3*sub(xi=+1,uu)+3*sub(xi=0,uu)-sub(xi=-1,uu))
109             +gamma^2*(u(j+2)-3*u(j+1)+3*u(j)-u(j-1));
110     llbc:=- (sub(xi=+1,uu)-3*sub(xi=0,uu)+3*sub(xi=-1,uu)-sub(xi=-2,uu))
111             +gamma^2*(u(j+1)-3*u(j)+3*u(j-1)-u(j-2));
112     ok:=if ok and(rrbc=0)and(llbc=0) then 1 else 0;
113     if disorder>5 then begin
114     rrrbc:=- (sub(xi=+3,uu)-5*sub(xi=+2,uu)+10*sub(xi=+1,uu)
115             -10*sub(xi=0,uu)+5*sub(xi=-1,uu)-sub(xi=-2,uu))
116             +gamma^3*(u(j+3)-5*u(j+2)+10*u(j+1)-10*u(j)+5*u(j-1)-u(j-2));

```

```

117     lllbc:=- (sub(xi=+2,uu)-5*sub(xi=+1,uu)+10*sub(xi=+0,uu)
118             -10*sub(xi=-1,uu)+5*sub(xi=-2,uu)-sub(xi=-3,uu))
119             +gamma^3*(u(j+2)-5*u(j+1)+10*u(j)-10*u(j-1)+5*u(j-2)-u(j-3));
120     ok:=if ok and(rrrbc=0)and(lllbc=0) then 1 else 0;
121     end;
122     end;
123     gd:=solg(deq,xi) +discof/h^disorder*
124         (if disorder=2 then (rbc-lbc) else
125             if disorder=4 then (rrbc-llbc) else
126                 if disorder=6 then (rrrbc-lllbc) );
127     gj:=gj+gd;
128     udash:=udash+h^disorder*solv(-deq+gd,xi)/discof
129     +(if disorder=2 then xi/2*(rbc+lbc) else
130         if disorder=4 then xi/2*(rbc+lbc)+xi^2/2*(rbc-lbc)
131             -(xi-xi^3)/12*(rrbc+llbc) else
132             if disorder=6 then xi/2*(rbc+lbc) +xi^2/2*(rbc-lbc)
133                 -(xi-xi^3)/12*(rrbc+llbc) -(xi^2-xi^4)/24*(rrbc-llbc)
134                 +(4*xi-5*xi^3+xi^5)/240*(rrrbc+lllbc) );
135     showtime;
136 end until ok or(iteration>25);
137
138 write deq:=deq;
139 write rbc:=rbc;
140 write lbc:=lbc;
141 write rrbc:=rbc;
142 write llbc:=lbc;
143 write rrrbc:=rbc;
144 write lllbc:=lbc;
145
146 end;

```

## References

- [1] D. Armbruster, J. Guckenheimer, and P. Holmes. Kuramoto–Sivashinsky dynamics on the centre-unstable manifold. *SIAM J. Appl. Math.*, 49:676–691, 1989. [http://locus.siam.org/SIAP/volume-49/art\\_0149039.html](http://locus.siam.org/SIAP/volume-49/art_0149039.html).
- [2] G. Berkooz, P. Holmes, and J. L. Lumley. The proper orthogonal decomposition in the analysis of turbulence. *Annu. Rev. Fluid Mech.*, 25:539–575, 1993. <http://arjournals.annualreviews.org/doi/abs/10.1146/annurev.fl.25.010193.002543>

- [3] J. Carr. *Applications of centre manifold theory*, volume 35 of *Applied Math. Sci.* Springer-Verlag, 1981.
- [4] J. Carr and R. G. Muncaster. The application of centre manifold theory to amplitude expansions. II. Infinite dimensional problems. *J. Diff. Eqns*, 50:280–288, 1983.
- [5] M. C. Cross and P. C. Hohenberg. Pattern formation outside of equilibrium. *Rev. Mod. Phys.*, 65(3):851–1112, 1993. [http://prola.aps.org/abstract/RMP/v65/i3/p851\\_1](http://prola.aps.org/abstract/RMP/v65/i3/p851_1).
- [6] H. Dankowicz, P. Holmes, G. Berkooz, and J. Elezgaray. Local models of spatio-temporally complex fields. *Physica D*, 90:387–407, 1996.
- [7] E. J. Doedel, R. C. Paffenroth, A. R. Champneys, T. F. Fairgrieve, Yu. A. Kuznetsov, B. Sandstede, and X. Wang. Auto 2000: Continuation and bifurcation software for ordinary differential equations (with HomCont). Technical report, Caltech, 2001.
- [8] B. Ermentrout. XPPAUT 5.0 - the differential equations tool. Technical report, [[http://www.math.pitt.edu/~bard/bardware/xpp\\_doc.pdf](http://www.math.pitt.edu/~bard/bardware/xpp_doc.pdf)], 2001.
- [9] C. Foias, M. S. Jolly, I. G. Kevrekidis, G. R. Sell, and E. S. Titi. On the computation of inertial manifolds. *Phys Lett. A*, 131:433–436, 1988.
- [10] C. Foias, M. S. Jolly, I. G. Kevrekidis, and E. S. Titi. On some dissipative fully discrete nonlinear galerkin schemes for the Kuramoto–Sivashinsky equation. *Phys. Lett. A*, 186(1):87, 1994.
- [11] C. Foias, B. Nicolaenko, G. R. Sell, and R. Teman. Inertial manifolds for the Kuramoto–Sivashinsky equation. *Comptes Rendus, Serie I*, 301:285–288, 1985. French.
- [12] P. Holmes, J. L. Lumley, and G. Berkooz. *Turbulence, Coherent Structures, Dynamical Systems and Symmetry*. Cambridge University Press, 1996.
- [13] J. M. Hyman and B. Nicolaenko. The Kuramoto–Sivashinsky equation: A bridge between pdes and dynamical systems. *Physica D*, 18:113–126, 1986.
- [14] M. S. Jolly, I. G. Kevrekidis, and E. S. Titi. Approximate inertial manifolds for the Kuramoto–Sivashinsky equation: analysis and computations. *Physica D*, 44:38–60, 1990.

- [15] I. G. Kevrekidis, B. Nicolaenko, and J. C. Scovel. Back in the saddle again: A computer assisted study of the Kuramoto–Sivashinsky equation. *SIAM J. Appl. Math.*, 50:760–790, 1990. [http://locus.siam.org/SIAP/volume-50/art\\_0150045.html](http://locus.siam.org/SIAP/volume-50/art_0150045.html).
- [16] Y. Kuramoto. Diffusion induced chaos in reactions systems. *Progr. Theoret. Phys. Suppl.*, 64:346–367, 1978.
- [17] S. J. Liao. The quite general BEM for strongly nonlinear problems. In Brebbia, Kim, Osswald, and Power, editors, *Boundary Elements XII*, pages 67–74. Computational Mechanics Publications, 1995.
- [18] T. Mackenzie and A. J. Roberts. Holistic finite differences accurately model the dynamics of the Kuramoto–Sivashinsky equation. *ANZIAM J.*, 42(E):C918–C935, 2000. <http://anziamj.austms.org.au/V42/CTAC99/Mack>.
- [19] Tony MacKenzie. Holistic discretisation accurately models complex dissipative spatio-temporal dynamical systems. PhD dissertation, in preparation.
- [20] M. Marion and R. Temam. Nonlinear Galerkin methods. *SIAM J. Numer. Anal.*, 26(5):1139–1157, 1989. [http://locus.siam.org/SINUM/volume-26/art\\_0726063.html](http://locus.siam.org/SINUM/volume-26/art_0726063.html).
- [21] Y. Pomeau and S. Zaleski. The Kuramoto–Sivashinsky equation: A caricature of hydrodynamic turbulence? *Lecture Notes In Physics*, 230, 1984.
- [22] A. J. Roberts. The utility of an invariant manifold description of the evolution of a dynamical system. *SIAM J. Math. Anal.*, 20:1447–1458, 1989. [http://locus.siam.org/SIMA/volume-20/art\\_0520094.html](http://locus.siam.org/SIMA/volume-20/art_0520094.html).
- [23] A. J. Roberts. Low-dimensional modelling of dynamical systems. Technical report, <http://arXiv.org/abs/chao-dyn/9705010>, 1997.
- [24] A. J. Roberts. Low-dimensional modelling of dynamics via computer algebra. *Computer Phys. Comm.*, 100:215–230, 1997.
- [25] A. J. Roberts. Holistic discretisation ensures fidelity to Burgers’ equation. *Applied Numerical Modelling*, 37:371–396, 2001.
- [26] A. J. Roberts. A holistic finite difference approach models linear dynamics consistently. *Mathematics of Computation*, 72:247–262, 2002. <http://www.ams.org/mcom/2003-72-241/S0025-5718-02-01448-5>.

- [27] A. J. Roberts. Derive boundary conditions for holistic discretisations of Burgers' equation. In K. Burrage and Roger B. Sidje, editors, *Proc. of 10th Computational Techniques and Applications Conference CTAC-2001*, volume 44, pages C664–C686, March 2003. <http://anziamj.austms.org.au/V44/CTAC2001/Robe>.
- [28] A. J. Roberts. Holistic discretisation of dynamical partial differential equations. Technical report, <http://www.sci.usq.edu.au/staff/aroberts/holistic.html>, April 2003. version 1.1.
- [29] J. C. Robinson. The asymptotic completeness of inertial manifolds. *Nonlinearity*, 9:1325–1340, 1996.
- [30] C. Scovel, I. G. Kevrekidis, and B. Nicolaenko. Scaling laws and the prediction of bifurcations in systems modeling pattern formation. *Phys. Lett. A*, 130:73–80, 1988.
- [31] G. I. Sivashinsky. Nonlinear analysis of hydrodynamic instability in laminar flames, part I: Derivation of the basic equations. *Acta Astronautica*, 4:1176–1206, 1977.
- [32] A. Vanderbauwhede. Centre manifolds. *Dynamics Reported*, 2:89–169, 1989.